A High-performing, Visible-light Driven Actuating Material Responsive to Ultra-low Light Intensities

Kin Wa Kwan, and Alfonso Hing Wan Ngan*

Dr K.W. Kwan 1, Prof. A.H.W. Ngan 1
Department of Mechanical Engineering,
The University of Hong Kong,
HKSAR

E-mail: kkwkwan@connect.hku.hk

Keywords: actuators, visible-light actuation, cobalt oxide, cobalt hydroxide, low light intensity

Light-driven actuating materials are highly desirable for miniaturized, untethered devices and microrobots. However, current light-actuators require high light intensity or the use of UV or IR light to operate, which greatly increase the cost and difficulty for real-life applications. Here, a significant visible (Vis) light-driven actuation effect in cobalt oxides/hydroxides (C-O-H), inducible at low intensities from ~3 mW/cm^2 (~0.03 sun), is reported. In the form of bilayered films, the actuators can curl into loops at 70 – 180 ms per loop, corresponding to a high intrinsic strain of more than 1% at strain rate 0.6%/s, and actuating stress exceeding 60 MPa, at ~50 mW/cm^2 (~0.5 sun). Linear actuators made from actuating hinges of C-O-H can weightlift objects ~200 times heavier than the active material. A chemo-mechanics model describes the actuation well, showing that the mechanism is light-induced volume shrinkage assisted by diffusion, and C-O-H exhibits outperforming chemical driving force per unit light-intensity stimulation.

1. Introduction

Untethered robots and devices[1] are mainly battery-powered or magnetically driven. Although many light-induced actuating materials have been introduced in the past few decades and some applications have been proposed,[2] real-life applications are limited by either the poor actuation performance, the requirement of high light intensities, or the use of IR or UV light sources that

are costly and harmful to human beings in terms of raising photocarcinogenesis [3] and photokeratitis risks [4]. For example, photostrictive materials actuate with low strains of <0.2%[5]. For the recently introduced photostrictive strontium ruthenate that can actuate with a strain of ~1%, a high light intensity of >500 mW/cm^2 is required.[6] As for liquid crystal elastomer (LCE)-based light-induced actuators, a high strain of >20% is achievable, but the actuation is mostly induced by UV light with high intensities.[7] Another group of light actuators – carbon nanotubes and graphene oxides-based materials – show good actuation performance in terms of magnitude and speed but IR or high-intensity light is required.[8]

Here, we report a Vis-light-responsive material, namely, oxides/hydroxides of cobalt (C-O-H), which is actuatable at light intensities as low as 3 mW/cm^2, by the volume change resulted from photothermally induced water desorption. Supported by a nickel (Ni) substrate, C-O-H can significantly induce actuation by curling, giving an intrinsic actuation strain exceeding 1% with a fast strain rate of 0.6%/s at ~50 mW/cm^2, which represents better performance than other low-intensity Vis-light actuators as described below.[9] These show that C-O-H may solve the abovementioned problems for light actuators.

We further developed a chemo-mechanical model to describe the actuation of bilayered bending actuators. From the model a figure of merit is defined for the intrinsic actuation performance of the actuating material. The results show that this figure of merit for C-O-H is significantly higher than nickel hydroxides/oxyhydroxides (NHO) of our previous work[9d]. This paves a way to compare actuating materials in an intrinsic, normalized fashion which is useful for the development in the analysis and discussion of bilayered bending actuators.

2. Results

2.1. Synthesis and characterization of C-O-H

By three-step electrodeposition, films with Ni substrate (thickness h_s = 1.2 μm), gold (Au) intermediate layer and C-O-H were electrodeposited on fluorine-doped tin oxide (FTO) glass

with areas of 2.2 × 0.2 cm^2. The deposition time of C-O-H was varied to obtain different thicknesses (h_a) (Figure S1). The films were peeled off from the FTO and clamped on one end for the actuation test. The microstructure of C-O-H observed in scanning electron microscopy (SEM) is rough and cracked which forms a bilayered structure with Ni (**Figure 1**b). The thin Au layer (<200 nm thick), which serves to improve the adhesion between C-O-H and Ni, is identified in energy-dispersive X-ray spectroscopy (EDS) (Figure S2). From EDS, only Co and O can be found in C-O-H as hydrogen is undetectable (Figure S3 and Table S1).

Broad diffraction peaks are found in glazing incidence X-ray diffraction (GIXRD) on C-O-H, indicating a turbostratic structure[10] (Figure 1c, blue arrows). These match the cobalt oxides (Co_3O_4 and CoO_2), hydroxide ($Co(OH)_2$) and oxyhydroxide (CoOOH) (Table S2). Selected area electron diffraction (SAED) on C-O-H shows dispersed diffraction rings, (Figure S4), and the measurable interplanar distances (~2.4 and ~1.5 Å) roughly match the GIXRD peaks at 2θ = ~38° and ~66°. Cyclic voltammetry (CV) in 1 M sodim hydroxide (NaOH) shows the characteristic oxidation peaks of cobalt oxides, hydroxide and oxyhydroxide[11] (Figure S5, red arrows), which can be attributed to the redox reactions listed in Table S3. However, electrochemically oxidized samples exhibit similar GIXRD results (Figure S6), indicating that the crystallinity or structural change accompanying the redox reaction is minor. From such characterization, the material is identified as Co-oxides/hydroxides (C-O-H). For simplicity, oxyhydroxide is regarded as a compound of oxide and hydroxide and is not included in the abbreviation.

2.2. Vis-light Induced Actuation of C-O-H

On illumination by low-intensity Vis-light, C-O-H undergoes contraction that drives the bilayered film structure to bend and curl. This is achievable by low-power commercially available LEDs as shown in Figure 1d (at ~3 mW/cm^2 with h_a = 1.6 μm). Increasing the intensity strengthens the actuation in terms of magnitude and speed (Video S1). The illumination and

recovery durations are carefully chosen for different intensities, so that the actuators can almost actuate to the maximum magnitude and recover completely. At 50 mW/cm^2, the lag time of actuation after stimulation is <70 ms, and only 70 – 180 ms is required to curl every loop (Figure 1e). The actuator starts recovery once the illumination is switched off, taking 8 s to fully recover in this example. To quantify the actuation, the curvature change κ of the actuator was measured. The average actuation stress $\bar{\sigma}_a$ exerted by C-O-H, derived in Supporting Information 3a, is proportional to κ as given by:

$$\bar{\sigma}_a = \frac{E_a h_a^3 + E_s h_s^3}{6 h_a (h_a + h_s)} \kappa \quad (1)$$

where E_a, E_s and h_a, h_s are the Young's modulus and thickness of C-O-H layer and Ni substrate. Both κ and $\bar{\sigma}_a$ increase linearly with light intensity; for the particular actuator shown in Figure 1d with h_a = 1.6 μm and h_s = 1.2 μm, κ increases from 500 to 1500 m^{-1} and $\bar{\sigma}_a$ from 8.3 to 24.9 MPa, as the light intensity increases from 3 to 50 mW/cm^2 (Figure 1f). The intrinsic actuation strain ε_a^{chem} of C-O-H, given by

$$\varepsilon_a^{chem} = -\bar{C}_a \bar{\sigma}_a \quad (2)$$

Where

$$\bar{C}_a = \frac{1}{E_a} + \frac{h_a}{E_s h_s} + \frac{3 h_a (h_a + h_s)^2}{E_a h_a^3 + E_s h_s^3} \quad (3)$$

and the average strain rate (dividing ε_a^{chem} by the total actuation time) also increase with light intensity; for the actuator shown in Figure 1d, these increase from -0.12 to -0.37% and -0.02 to -0.37%/s, respectively (Figure 1g, negative values indicate compressive strain). The recovery time also increases with light intensity. While the actuator takes ~4 s to recover from illumination at 10 mW/cm^2, ~8 s is needed from 50 mW/cm^2. Note that as the actuator was curly at room temperature and laboratory relative humidity (RH) of 60%, it was straightened in a humid container (RH = 95%) during the tests. The actuation of C-O-H shows good repeatability with only minor deterioration over 5000 cycles (Figure S8, h_a = 1.6 μm). Video S2 shows that on prolonged cyclic testing, the actuator's recovery became more sluggish so that

it did not have enough time to recover to the initial straight shape during each cycle. However, by resting for 1 h, the actuator straightened again, and the performance was restored.

Actuation of the bilayered actuator configuration depends strongly on the C-O-H thickness h_a. As slower actuation is found for higher h_a (Video S3), prolonged illumination was applied. The results show that κ first increases with h_a and then decreases to a constant value (Figure S12a). At the highest intensity tested (50 mW/cm^2), ε_a^{chem} increases with h_a from -0.54% to -1.29%, and $\bar{\sigma}_a$ first decreases rapidly from 63 to 24 MPa and then increases slowly to 41 MPa with h_a. Figure 1h shows the variation of $\bar{\sigma}_a$ against ε_a^{chem} from the data of Figure S12c and 12e, which show that at low h_a, ε_a^{chem} is relatively constant for various $\bar{\sigma}_a$. However, ε_a^{chem} increases rapidly with $\bar{\sigma}_a$ at high h_a. This shows that the actuation behaviour is different in low and high h_a regimes (see Supporting Information 3a for detailed explanation). Comparing with other Vis-light actuators at low intensity, C-O-H produces significantly faster actuation (~100 ms vs 5 s[9c] for a displacement of 2 mm) and larger magnitude (~2500 m^{-1} vs ~300 m^{-1} in curvature;[9b] actuation strain ~1% vs ~0.3%[9a, 9d]). The actuating work density calculated by Equation S16 is 0.07 to 0.27 MJ/m^3 or 10 to 70 J/kg (density of oxides and hydroxides of cobalt: 3.6 – 5.9 g/cm^3) and the power density is estimated to be ~30 W/kg, which compares favourably with other actuating materials.[12]

2.3. Actuation Mechanism of C-O-H

The actuation mechanism is found to be water desorption. As shown in Figure S14, actuation can be induced by lowering the RH. Further illuminating the actuators shows that the light-stimulated actuation decreases as RH decreases (**Figure 2**a and Video S4). Therefore, it is believed that C-O-H expands/contracts under water adsorption/desorption. Mass measurement by quartz crystal microbalance shows a mass increase in C-O-H when the environment is moisturized and a decrease when illuminated (Figure 2b), proving that illumination causes desorption of water from C-O-H. As the actuation is also inducible by temperature increase

(from room temperature to 50°C in Figure 2c) and by illuminating the Ni substrate instead of C-O-H (Figure 2d), it is believed that the light-induced water desorption is caused by photothermal effect (Video S5). This also agrees with the phenomenon of thermal removal of adsorbed water from cobalt hydroxide.[13]

Actuators with thicker C-O-H layers typically exhibit an initial fast actuation response followed by a slowed-down response, as shown by the example in the inset of Figure 2e and Video S6 for the case of h_a = 4.5 μm. The linear plot of the square root of total actuation time against h_a (Figure 2e) suggests that the slow response is governed by water diffusion. From this we deduce that the incident Vis-light can only penetrate a surface layer with a small thickness h_t from which water is desorbed, whereas the underlying layer of C-O-H (of thickness h_a - h_t) is not stimulated by light, but the water content there gradually diffuses to the top layer at which it is removed by light activation. The fast response therefore corresponds to the stage when water is removed quickly by light from the top layer to cause it to shrink, but diffusion and hence shrinkage have not yet been significant in the diffusive layer. As shown in Supporting Information 3b (Equation S27), the curvature of the fast actuation is given by

$$\kappa_{fast} = \frac{6h_t(Y_2 - h_t Y_1)}{\Delta E\left(E_a h_a^4 - E_s h_s^4\right) + E_a E_s h^4 + h_t E_a(-4Y_3 + 6h_t Y_2 - 3h_t^2 Y_1)} \bar{\sigma}_{a,fast} \qquad (4)$$

where $\Delta E = E_a - E_s$; $h = h_a + h_s$; $Y_n = \Delta E h_a^n + E_s h^n$. If $h_t = h_a$, then Equation 4 reduces to Equation 1. Figure 2f shows that by selecting the value h_t = 1.36 μm, the plot of κ_{fast} vs the factor on the right side of Equation 4 would exhibit the highest linearity. The thickness of h_t = 1.36 μm is therefore an estimate of the penetration depth of 50 mW/cm^2 Vis-light into C-O-H that would cause rapid water desorption. The average actuation stress $\bar{\sigma}_{a,fast}$ for the fast response of the light-triggered C-O-H layer can also be estimated from the slope of the best fitting line in Figure 2f to be 33.2 MPa, which agrees in magnitude with the $\bar{\sigma}_a$ of active layers with h_a values similar to h_t in Figure 1f. Although governed by diffusion, the actuation rate is still fast compared with many other actuators, which require >5s to completely actuate.[7d, 9b, 9c, 14]

2.4. Demos of Application – Weightlifting Actuators

By selectively electrodepositing C-O-H onto the Ni substrate (**Figure 3**a), an actuating hinge can be made. Such a hinge can weightlift an object equivalent to ~150 – 250 times the weight of C-O-H layer (Video S7, mass of the object: 34 mg, volume of C-O-H: $0.4\times0.6\times1.6\times10^{-4}$ cm^3, tests carried out in 80% RH to show that the actuator can work in a drier environment) The device strain, defined as the ratio of the distance lifted *D* to the length *L* of the device, increases from ~20 to ~40% as the light intensity increases from 10 to 50 mW/cm^2 (Figure 3d). By assembling 3 actuators with double actuating hinges, an object of 110 mg can be lifted (Figure 3b). Despite under an even drier environment at 60% RH, device strains of ~10 – ~20% were achieved (Figure 3e), and by adding a droplet of water at the position shown in Figure 3b, the device strain increases significantly to ~30% at 20 mW/cm^2 illumination (Video S8). This shows that a minute amount of water can greatly enhance the performance in an otherwise dry environment. Beside illumination, Joule heating can also actuate C-O-H. Figure 3c and Video S9 show an Ni substrate made into a U-shape for conducting electrical currents, enabling the hinges to weightlift an object under 1.1 V repeatedly (Figure 3f).

2.5. Chemo-mechanics Model on the Actuation

Lastly, a chemo-mechanics model is developed to quantify the light-triggered actuation of C-O-H (Supporting information 4a). Depicting the actuation as a stress-assisted chemical reaction between the water-desorbed, smaller state and the water-adsorbed, larger state of C-O-H, namely, C-O-H(smaller, water desorbed) ⇌ C-O-H(larger, water adsorbed), with ΔE_{chem} being the chemical driving force provided by light stimulation to desorb water and shrink C-O-H as shown in **Figure 4**a, the equilibrium constant of this chemical reaction corresponds to a strain ε_a^{chem} that is given by (Equation S31):

$$\sigma_a \Omega \approx \Delta E_{chem} + 3kT\varepsilon_a^{chem} \quad (5)$$

where σ_a, unlike the $\bar{\sigma}_a$ in Equation 2 which is the average stress in the active layer, is the stress in the top surface of the active layer that is triggered by light, and Ω is an activation volume. On the other hand, treating the mechanics of the actuation as elastoplasticity with the plastic actuation ε_a^{chem} in series with the bending elasticity of the bilayered system as shown in Figure 4a, σ_a and ε_a^{chem} are related by (Supporting Information 4c):

$$\varepsilon_a^{chem} = -\left[\frac{\frac{(h_a+h_s)}{2}+\frac{E_a h_a^3+E_s h_s^3}{6(h_a+h_s)}\left(\frac{1}{E_a h_a}+\frac{1}{E_s h_s}\right)}{\frac{E_a h_a^3+E_s h_s^3}{6h_a(h_a+h_s)}-\frac{E_a h_a}{2}}\right]\sigma_a \quad (6)$$

Chemo-mechanical equilibrium is therefore established when Equation 5 and 6 are satisfied simultaneously. Combining Equation 1, 2, 3, 5 and 6, a normalized curvature $K = \kappa(E_s h_s^3)^{1/3}/(\phi E_a^{1/3})$ can be defined to represent the actuation performance, which is given by

$$K = \frac{\kappa h_s}{\phi\,\beta^{1/3}} = \frac{6\alpha\beta^{2/3}(1+\alpha)}{(1+\alpha\beta)(1+\alpha^3\beta)+\omega[1-\alpha^2\beta(3+2\alpha)]+3\alpha\beta(1+\alpha)^2} \quad (7)$$

where $\alpha = h_a/h_s$, $\beta = E_a/E_s$, $\phi = \Delta E_{chem}/(3kT)$, and $\omega = E_a\Omega/(3kT)$. K here is a normalized measure for curvature performance because a higher K means (i) higher substrate bending stiffness $E_s h_s^3$ for the same curvature κ, (ii) higher curvature κ for the same substrate bending stiffness $E_s h_s^3$, and (iii), lower driving force ϕ needed for the same curvature and substrate bending stiffness.

Figure S17b shows ε_a^{chem} plotted against σ_a/E_a, calculated from the same curvature data (κ) from which Figure 1h is plotted, and the data on another actuating material nickel hydroxide-oxyhydroxide (NHO) fabricated for comparison.[9d] According to Equation 5, the y-intercept gives the normalized driving force ϕ, from which the normalized curvatures K in Equation 7 can be calculated from the experimentally measured curvatures κ. The K values obtained this way are plotted as discrete points in Figure 4b against $\alpha = h_a/h_s$. Also shown in Figure 4b are the theoretical trends according to the right side of Equation 7 with envelop values of ω of 0 to 1. It can be seen that most of the experimental data are well describable by the theoretical trends; the only exception is one data point for NHO at 10 mW/cm^2, which can be fitted by a ω value of 2. Figure S18 shows the theoretical plot of $K(\alpha, \beta)$ according to Equation 7 at an indicative

value of ω = 0.5, and the cross-sections for C-O-H and NHO with β of 0.077 and 0.11 respectively.

In summary, C-O-H and NHO have a similar range of ω within ~0 to 1, which translates into an activation volume Ω from 0 (i.e. actuation being stress-independent) up to ~0.7 Å^3. Although the $K(\alpha)$ plots are similar because the values of β and ω are similar for C-O-H and NHO, C-O-H has significantly higher ϕ values than NHO as shown in Figure 4c. As K equals $\kappa h_s/(\phi\beta^{1/3})$, even though both materials have similar K at the same α, a higher ϕ means that the actuation curvature κ for C-O-H is higher at the same thickness ratio α and light intensity. C-O-H also has significantly higher work and power density than NHO (70 J/kg vs 20 J/kg and ~30 W/kg vs ~10 W/kg). Furthermore, C-O-H can be coated to much higher thickness than NHO (maximum thicknesses of ~10 μm and ~2 μm respectively), which means that C-O-H can be used to drive much thicker substrates than NHO. This may be useful in real-life applications where thicker substrates have to be used due to the fabrication difficulties of thin substrates. All in all, the present results indicate that C-O-H significantly outperforms NHO as a Vis-light triggered actuating material.

3. Conclusion

In conclusion, C-O-H shows significant actuation which is better than photostrictive materials[5] and is comparable to carbon nanotubes and graphene oxides-based actuators[8]. Despite having a weaker performance than LCE-based actuators[7], the fact that C-O-H being actuatable by Vis-light at low intensity, the easy fabrication by electrodeposition, and the possibility to make into different shapes as shown in the demonstrations show the advantages of the material. Also, comparing to our previous work on NHO, C-O-H shows higher actuation strain and is more actuatable by low light intensities as shown above. The chemo-mechanical model developed in this work gives an equation (Equation 7) that can well describe the experimental results of C-O-H and NHO actuation in Figure 4. The normalized driving force ϕ, which is a figure of merit

of the light-induced actuation, will be useful for further development and future applications of the material.

4. Experimental Section

Chemicals and Materials: A commercial Ni-plating kit (Caswell Inc.) was used to prepare the solution bath for electrodepositing nickel (Ni). An Oromerse SO Part B (Technic Inc.) electroless plating solution was used for preparing the Au bath. For the solution bath for electrodepositing cobalt oxides/hydroxides (C-O-H), the chemicals were used as purchased from Sigma-Aldrich without further purification. Cobalt sulfate heptahydrate ($CoSO_4 \cdot 7H_2O$) ReagentPlus®, ≥99%, sodium acetate (CH_3COONa) and sodium sulfate (Na_2SO_4) in puriss. p.a., anhydrous, and sodium hydroxide (NaOH) in puriss. p.a., ≥98%, pellets were used.

Fluorine-doped tin oxide (FTO)-coated glass slides (2.3 mm thick; sheet resistance, ~10 ohms/square) were purchased from Sigma-Aldrich. Chemical-resist stickers (50 mm thick; CM-200E) were purchased from MAX Bepop, and copper (Cu) tape was purchased from 3M. Deionized (DI) water with a resistivity of ~18 megohms·cm was used to make all the solution baths and for rinsing.

Three-step electrodeposition of C-O-H film actuator: First, Ni was electrodeposited on FTO glass masked by a chemical-resist sticker with rectangular openings (the typical size was 22 mm by 2 mm), using a constant cathodic current of −15 mA/cm^2 for 5 min in the Ni bath in a two-electrode electrochemical cell against a Ni metal sheet counter electrode. To enable the C-O-H to firmly adhere on Ni, a thin Au layer was electrodeposited on the Ni. The Au bath was composed of Oromerse SO Part B and 1.7 M sodium sulfite (Na_2SO_3) in the volume ratio of 1:9, and a constant cathodic current density of −0.1 mA/cm^2 was applied to the Ni-plated FTO in a two-electrode cell against a platinum (Pt) mesh counter electrode for 30 min. Lastly, C-O-H was anodically electrodeposited on the substrate in a solution bath of $CoSO_4 \cdot 7H_2O$, CH_3COONa, and Na_2SO_4, all at 0.05 M, in a three-electrode cell. The current density was

0.545 mA/cm^2 against saturated calomel reference electrode (SCE) and Pt mesh counter electrode for various electrodeposition durations under vigorous stirring. After each plating process, the sample and the FTO glass were rinsed with DI water and dried in air. After the three-step electrodeposition process, the resultant film actuator was peeled off from the FTO glass by a pair of sharp tweezers. For the rectangular actuators with the size of 22 mm by 2 mm, one end of the film actuator was adhered to a piece of Cu tape so that it could be clamped for the actuation tests and electrochemical characterization. This reduced the exposed size of the actuator to about 20 mm by 2 mm.

Materials characterization of C-O-H: Scanning electron microscopy (SEM) and energy-dispersive X-ray spectroscopy (EDS) were carried out in a LEO 1530 FEG scanning electron microscope. Samples were prepared by directly cutting small pieces from film actuators and adhering them to sample holders. For imaging, the samples were gold-palladium (Au-Pd) sputtered for 20 s in a Bal-Tec SCD 005 Sputter Coater. For EDS, no sputtering was performed. Selected area electron diffraction (SAED) were carried out in an FEI Tecnai G220 S-TWIN STEM. Samples were prepared by direct plating C-O-H onto FTO glass plates, with the same fabrication methods described above. Then, the C-O-H was scratched off the FTO by sharp tweezers and adhered to a TEM Cu grid with carbon film wetted with DI water. Glazing incidence X-ray diffraction (GIXRD) was performed in a Rigaku SmartLab 9-kW X-ray diffractometer. Samples were prepared by the same fabrication methods described above. Samples supported on FTO glass were put directly onto the sample holder of the diffractometer. Parallel-beam/parallel-slit analyser mode was used, with the incident angle for the x-ray beam being 0.5° and the sweep rate being 0.3°/min at steps of 0.1°. Cyclic voltammetry characterization was performed to actuators by CS350 single channel potentiostat (Corrtest) against an Ag/AgCl reference electrode and a Pt mesh counter electrode in 1 M NaOH. To prevent any contact of the Cu tape to the solution, a thin coating of lacquer was applied to the tape for insulation. The potential window was -0.5 to 0.5 V with a scan rate of 1 mV/s.

Light-induced actuation tests: Actuation tests were performed inside a compartment illuminated by low-intensity light-emitting diode (LED) video light (LEDP260C, Godox) as background lighting for photography and video recording. The wavelength of white light is checked by a spectrometer (HR2000 + CG, Ocean Optics) to be 400 to 700 nm, that of blue, green and red LED light was measured to be about 400, 520, and 700 nm. Temperature is measured by infrared laser thermometer (Fluke, 62 MAX+). Curvature κ of actuators at initial and actuated states were measured from the recorded videos and assume the shapes of bent or curled actuators to be circular. For lightly bent actuator, κ was calculated by $\kappa = 2x/(x^2 + y^2)$, where (x, y) are the coordinates of the free end relative to the clamped end of actuators. For actuation more than 1 loop, $\kappa = 2n\pi/(L - L_0)$ is used, where n is the number of loops curled, L is the length of the actuator and L_0 is the length of the actuator that was not actuated due to blockage of light illuminated or other reasons.

Supporting Information

Supporting Information is available from the Wiley Online Library or from the author.

Acknowledgements

We thank F. Y. F Chan for the operation of TEM, and K. Mu for the operation of QCM. This work was funded by a grant from the Research Grants Council (project no. 17206114) of the Hong Kong Special Administrative Region and the Kingboard Endowed Professorship in Materials Engineering. K.W.K. and A.H.W.N. conceived the idea, designed the experiments, and wrote the manuscript. K.W.K performed the experiments. All the authors contributed materials and/or tools and analyzed the data. The authors declare that they haveno competing interests.

Received: ((will be filled in by the editorial staff))
Revised: ((will be filled in by the editorial staff))
Published online: ((will be filled in by the editorial staff))

References

[1] a) S. Miyashita, S. Guitron, M. Ludersdorfer, C. R. Sung, D. Rus, "An untethered miniature origami robot that self-folds, walks, swims, and degrades", presented at *2015 IEEE International Conference on Robotics and Automation (ICRA)*, 2015; b) Y. Kim, H. Yuk, R. Zhao, S. A. Chester, X. Zhao, *Nature* **2018**, *558*, 274; c) W. Hu, G. Z. Lum, M. Mastrangeli, M. Sitti, *Nature* **2018**, *554*, 81; d) N. T. Jafferis, E. F. Helbling, M. Karpelson, R. J. Wood, *Nature* **2019**, *570*, 491.
[2] a) H. Zeng, P. Wasylczyk, C. Parmeggiani, D. Martella, M. Burresi, D. S. Wiersma, *Adv. Mater.* **2015**, *27*, 3883; b) M. Rogóż, H. Zeng, C. Xuan, D. S. Wiersma, P. Wasylczyk, *Adv. Opt. Mater.* **2016**, *4*, 1689; c) O. M. Wani, H. Zeng, A. Priimagi, *Nat. Commun.* **2017**, *8*, 15546.
[3] a) S. M. Schieke, P. Schroeder, J. Krutmann, *Photodermatology, photoimmunology & photomedicine* **2003**, *19*, 228; b) S. Cho, M. H. Shin, Y. K. Kim, J.-E. Seo, Y. M. Lee, C.-H. Park, J. H. Chung, *Journal of Investigative Dermatology Symposium Proceedings* **2009**, *14*, 15.
[4] a) R. M. Lucas, *Eye & contact lens* **2011**, *37*, 168; b) J. Parrish, *UV-A: Biological effects of ultraviolet radiation with emphasis on human responses to longwave ultraviolet*, Springer Science & Business Media, 2012.
[5] K. Uchino, in *Advanced Piezoelectric Materials*, Elsevier, 2017, 755.
[6] T.-C. Wei, H.-P. Wang, H.-J. Liu, D.-S. Tsai, J.-J. Ke, C.-L. Wu, Y.-P. Yin, Q. Zhan, G.-R. Lin, Y.-H. Chu, *Nat. Commun.* **2017**, *8*, 15018.
[7] a) C. L. Van Oosten, C. W. Bastiaansen, D. J. Broer, *Nat. Mater.* **2009**, *8*, 677; b) S. Iamsaard, S. J. Aßhoff, B. Matt, T. Kudernac, J. J. Cornelissen, S. P. Fletcher, N. Katsonis, *Nat. Chem.* **2014**, *6*, 229; c) T. J. White, D. J. Broer, *Nat. Mater.* **2015**, *14*, 1087; d) M. Lahikainen, H. Zeng, A. Priimagi, *Nat. Commun.* **2018**, *9*, 4148.
[8] a) E. Wang, M. S. Desai, S.-W. Lee, *Nano Lett.* **2013**, *13*, 2826; b) M. Ji, N. Jiang, J. Chang, J. Sun, *Adv. Funct. Mater.* **2014**, *24*, 5412; c) J. Mu, C. Hou, H. Wang, Y. Li, Q. Zhang, M. Zhu, *Sci. Adv.* **2015**, *1*, e1500533; d) H. Arazoe, D. Miyajima, K. Akaike, F. Araoka, E. Sato, T. Hikima, M. Kawamoto, T. Aida, *Nat. Mater.* **2016**, *15*, 1084; e) Y. Hu, J. Liu, L. Chang, L. Yang, A. Xu, K. Qi, P. Lu, G. Wu, W. Chen, Y. Wu, *Adv. Funct. Mater.* **2017**, *27*, 1704388; f) P. Zhou, L. Chen, L. Yao, M. Weng, W. Zhang, *Nanoscale* **2018**, *10*, 8422.
[9] a) S. Lu, B. Panchapakesan, *Nanotechnology* **2005**, *16*, 2548; b) F. Cheng, R. Yin, Y. Zhang, C.-C. Yen, Y. Yu, *Soft Matter* **2010**, *6*, 3447; c) Q. Yu, X. Yang, Y. Chen, K. Yu, J. Gao, Z. Liu, P. Cheng, Z. Zhang, B. Aguila, S. Ma, *Angew. Chem. Int. Ed.* **2018**, *57*, 10192; d) K. Kwan, S. Li, N. Hau, W.-D. Li, S. Feng, A. H. Ngan, *Sci. Robot.* **2018**, *3*, eaat4051.
[10] C. Faure, C. Delmas, P. Willmann, *J. Power Sources* **1991**, *35*, 263.
[11] H. G. Meier, J. Vilche, A. Arvia, *J. Electroanal. Chem.* **1982**, *138*, 367.
[12] J. D. Madden, N. A. Vandesteeg, P. A. Anquetil, P. G. Madden, A. Takshi, R. Z. Pytel, S. R. Lafontaine, P. A. Wieringa, I. W. Hunter, *IEEE Journal of oceanic engineering* **2004**, *29*, 706.
[13] a) Y. Zhu, H. Li, Y. Koltypin, A. Gedanken, *J. Mater. Chem.* **2002**, *12*, 729; b) Z. Liu, R. Ma, M. Osada, K. Takada, T. Sasaki, *J. Am. Chem. Soc.* **2005**, *127*, 13869.

[14] L. Zhang, P. Naumov, *Angew. Chem. Int. Ed.* **2015**, *54*, 8642.

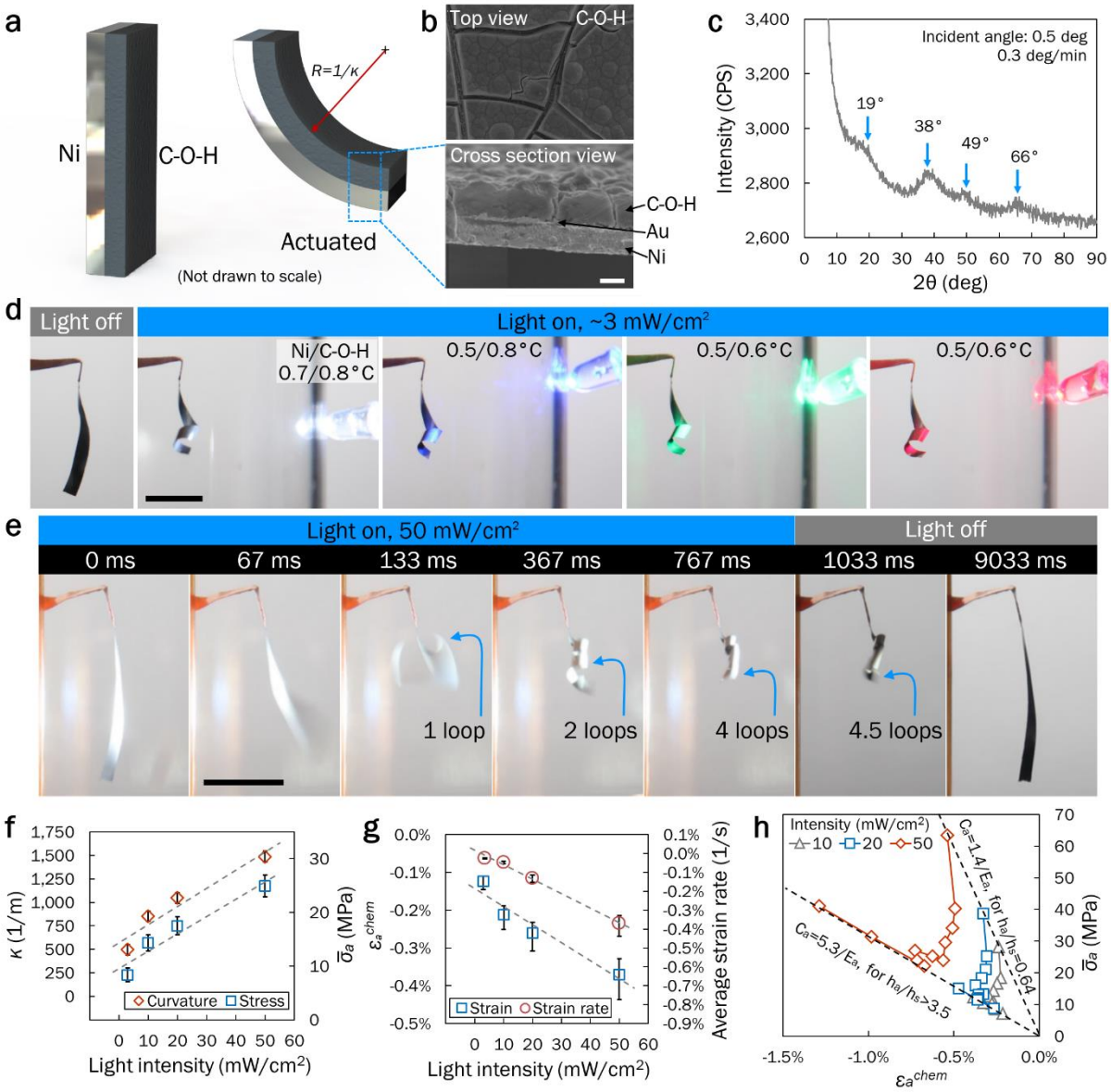

Figure 1. Material and actuation characterization of C-O-H. a) Schematic of C-O-H actuator characterised by curvature κ. b) SEM on top view and cross section view (scale bar: 2 μm) of C-O-H actuator. c) GIXRD of C-O-H. d)-g) Light actuation performance of the actuator in (b) (with h_a = 1.6 μm, h_s = 1.2 μm, and shorter illumination time just to achieve certain large actuation): d) snapshots of light actuation test induced by LEDs with different colours at ~3 mW/cm^2, with the temperature increase under illumination on Ni surface/C-O-H surface indicated (scale bar: 10 mm); e) snapshots of light actuation at 50 mW/cm^2 (scale bar: 10 mm); f) curvature κ and average actuation stress $\bar{\sigma}_a$ plotted against Vis-light intensity; g) intrinsic actuation strain ε_a^{chem} and average strain rate plotted against Vis-light intensity. h) Average

actuation stress against intrinsic actuation strain for actuators with h_a ranging from 0.8 to 9.4 μm on Ni substrates with thickness h_s = 1.2 μm under different light intensities and prolonged illumination to ensure full actuation.

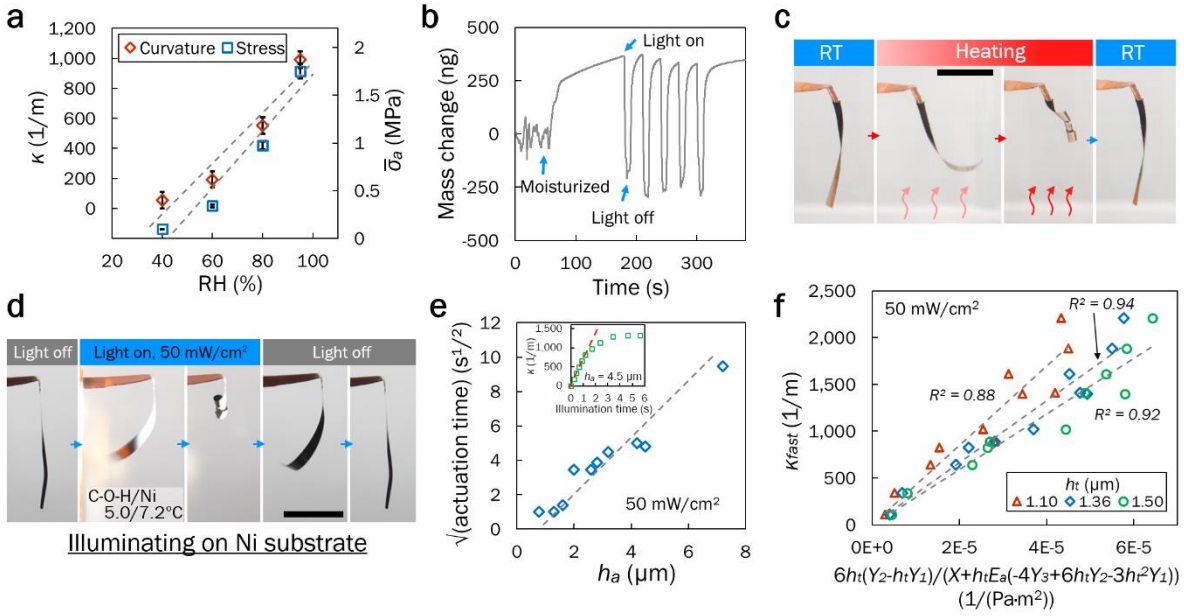

Figure 2. Mechanism of the light induced actuation. a) Curvature κ and average actuation stress σ_a plotted against RH. b) Mass measurement on moisturized and illuminated C-O-H by QCM. c) Actuation induced by heating by a hot plate, with the actuator contained in a sealed environment at 95% RH (scale bar: 10 mm). d) Light actuation induced by illuminating Ni substrate of the actuator from the right, with the temperature increase under illumination on C-O-H surface/Ni surface indicated (scale bar: 10 mm). e) Square root of total actuation time plotted against the thickness of the active layer h_a actuated at 50 mW/cm^2. Inset is a typical plot of curvature against illumination time for an actuator with h_a = 4.5 μm, showing an initial fast response followed by a slow one. f) Plot of curvature κ_{fast} at the end of the fast response against $[6h_t(Y_2 - h_tY_1)]/[X + h_tE_a(-4Y_3 + 6h_tY_2 - 3h_t^2Y_1)]$, for various h_t; the value h_t = 1.36 μm maximizes R^2.

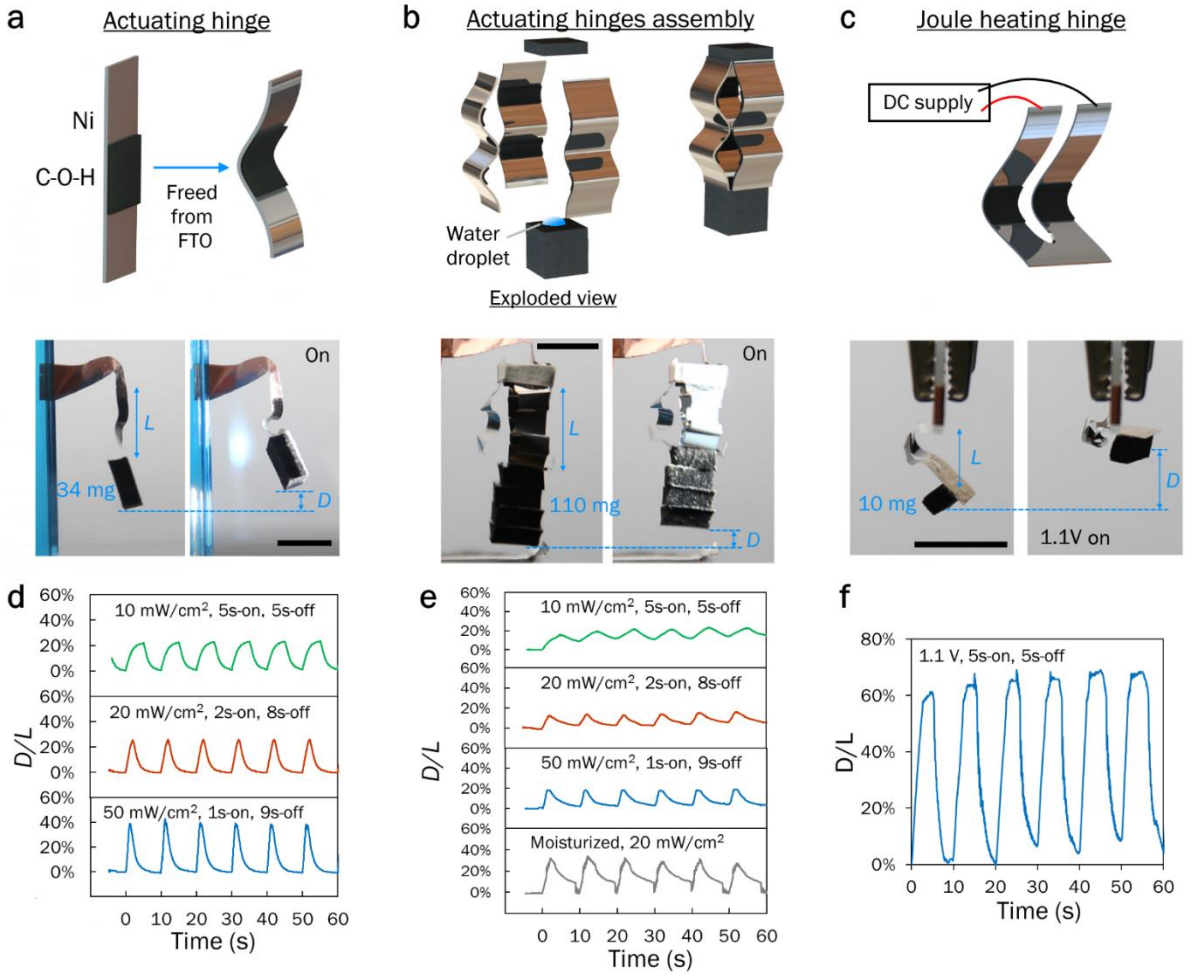

Figure 3. Weightlifting of C-O-H actuating hinges. Scheme diagram and snapshots of a) an actuating hinge (scale bar: 10 mm), b) an assembly of 3 actuators with double actuating hinges (scale bar: 10 mm), and c) U-shape hinge for Joule heating actuation. d)-f) The actuation performance plots corresponding to (a)-(c) – d) device strain *D/L* of the actuating hinge lifting an object of 34 mg at various light intensities at 80% RH, e) that of the actuator assembly lifting an object of 110 mg at 60% RH, and f) that of the U-shape hinge lifting an object of 10 mg under 1.1 V voltage at 60% RH.

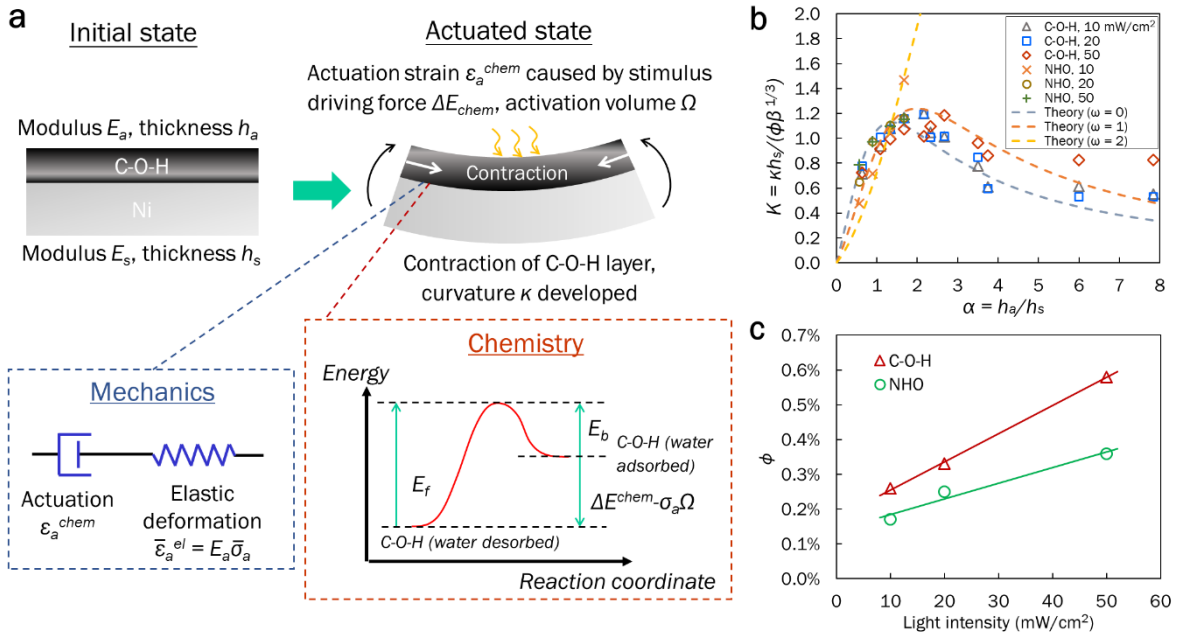

Figure 4. Quantitative actuation performance. a) Chemo-mechanics equilibrium for a bending actuator design. Stimulation provides chemical driving force ΔE_{chem} which leads to actuation strain ε_a^{chem}. Due to the constraint of the passive layer, stress σ_a is developed in the active material, which suppresses the actuation reaction via an activation volume Ω. b) A plot of $K = \kappa h_s/(\phi\beta^{1/3})$ against $\alpha = h_a/h_s$. Experimental values of K are calculated from the curvature values for C-O-H and NHO. Theoretical curves for different values of $\omega = E_a\Omega/(3kT)$ as per Equation 7 assume an average β value of 0.093 between C-O-H (β = 0.077) and NHO (β = 0.11). c) Normalized driving force $\phi = \Delta E_{chem}/(3kT)$ at different light intensities.

Table of contents

A bilayered actuator consists of an active layer of cobalt oxides/hydroxides and nickel substrate is developed. The active layer contracts under low-intensity visible-light through water desorption, resulting large actuation movement in high speed. It stands out from other light actuators which either require IR or UV to function or have weaker performances.

Keyword: actuator

Kin Wa Kwan, and Alfonso Hing Wan Ngan*

A High-performing, Visible-light Driven Actuating Material Responsive to Ultra-low Light Intensities

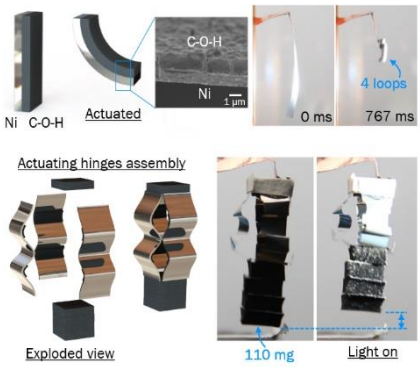

Supporting Information

A High-performing, Visible-light Driven Actuating Material Responsive to Ultra-low Light Intensities

Kin Wa Kwan, and Alfonso Hing Wan Ngan*

1. Supporting Figures and Tables

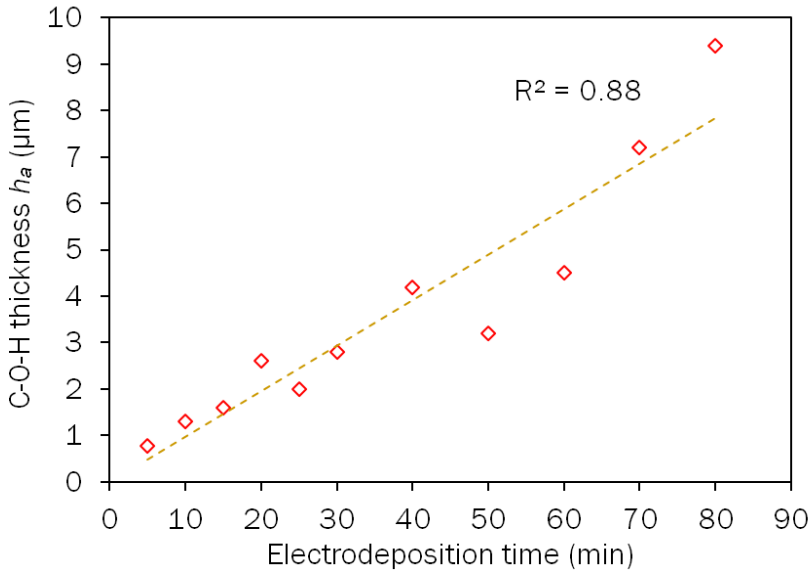

Figure S1. C-O-H thickness h_a versus electrodeposition time.

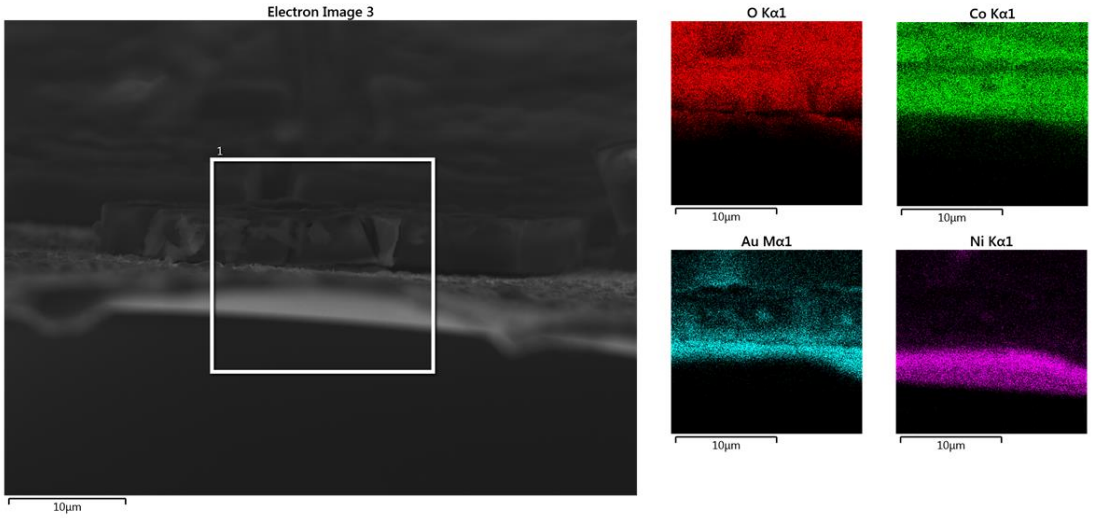

Figure S2. EDS mapping on a cross section of C-O-H.

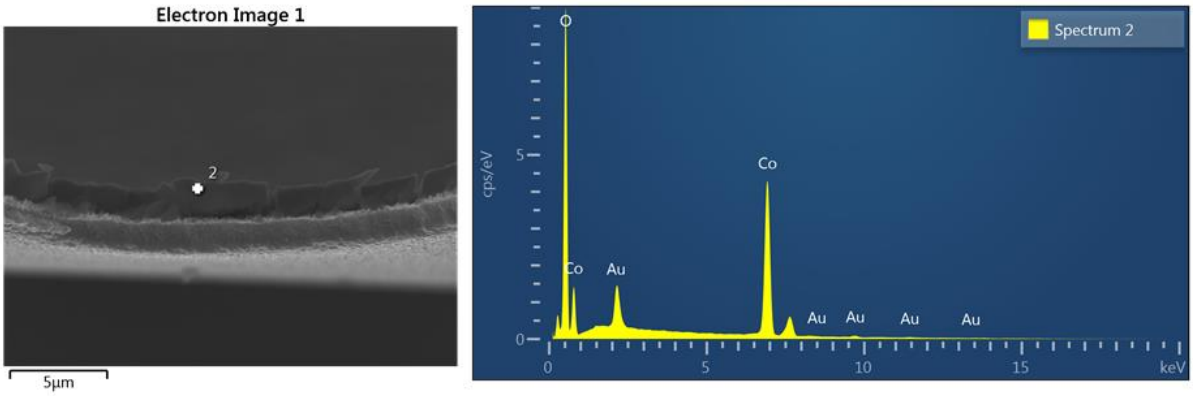

Figure S3. Single point EDS on a cross section of C-O-H.

Element	Wt%	Atomic %
O	27.23	59.81
Co	65.09	38.82
Au	7.68	1.37
Total:	100.00	100.00

Table S1. Weight percentage and atomic percentage of C-O-H layer from single point EDS in Figure S3.

2θ	**$Co(OH)_2$[1]**	**CoOOH[2]**	**Co_3O_4[3]**	**CoO_2[4]**
19°	(001),	(0003)	(111)	(200)
38°	(111)	$(10\bar{1}2)$	(311)	(211)
49°	(112)	$(10\bar{1}5)$	/	(411)
66°	$(11\bar{3})$	$(2\bar{1}\bar{1}0)$	(440)	/

Table S2. Possible planes that match the GIXRD peaks in Figure 1c.

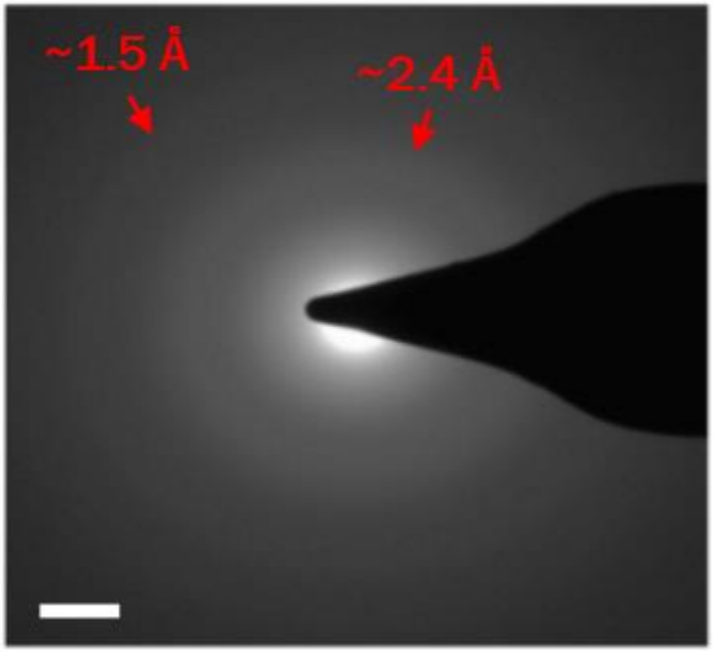

Figure S4. Selected area electron diffraction (SAED) of C-O-H. (scale bar: 2 1/nm)

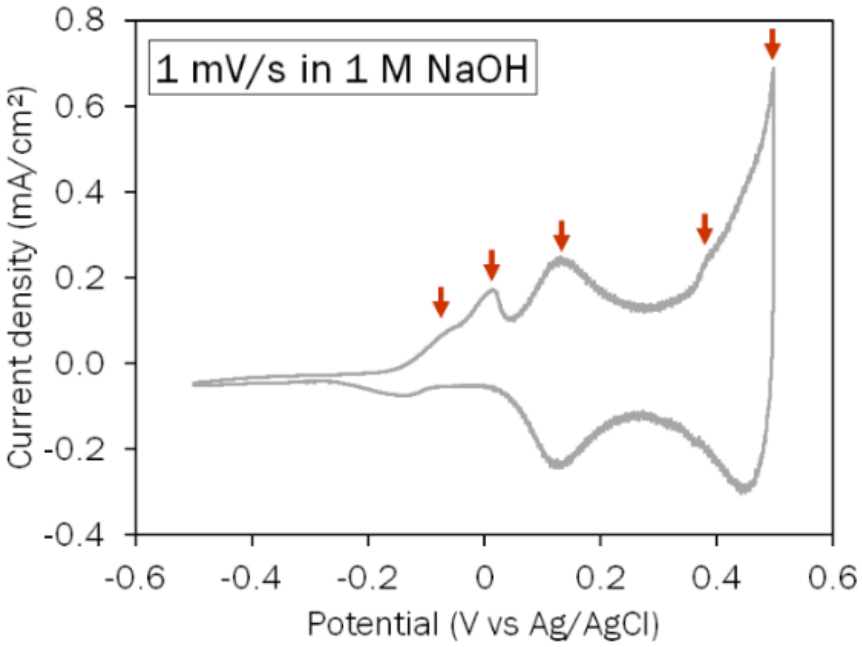

Figure S5. Cyclic voltammetry (CV) of C-O-H under 1 M NaOH at 1 mV/s.

Potential [V vs Ag/AgCl]	Redox reactions[5]
-0.07	$Co(OH)_2 + OH^- \leftrightarrow CoOOH + H_2O + e^-$
-0.02 and 0.13	$Co_3O_4 + OH^- + H_2O \leftrightarrow 3CoOOH + e^-$
	$Co(OH)_2 + 2OH^- \leftrightarrow CoO_2 + 2H_2O + 2e^-$
0.39	$Co_3O_4 + 4OH^- \leftrightarrow 3CoO_2 + 2H_2O + 4e^-$
0.50	$CoOOH + OH^- \leftrightarrow CoO_2 + H_2O + e^-$

Table S3. Redox reactions that may occur at the redox peaks in the CV shown in Figure S5.

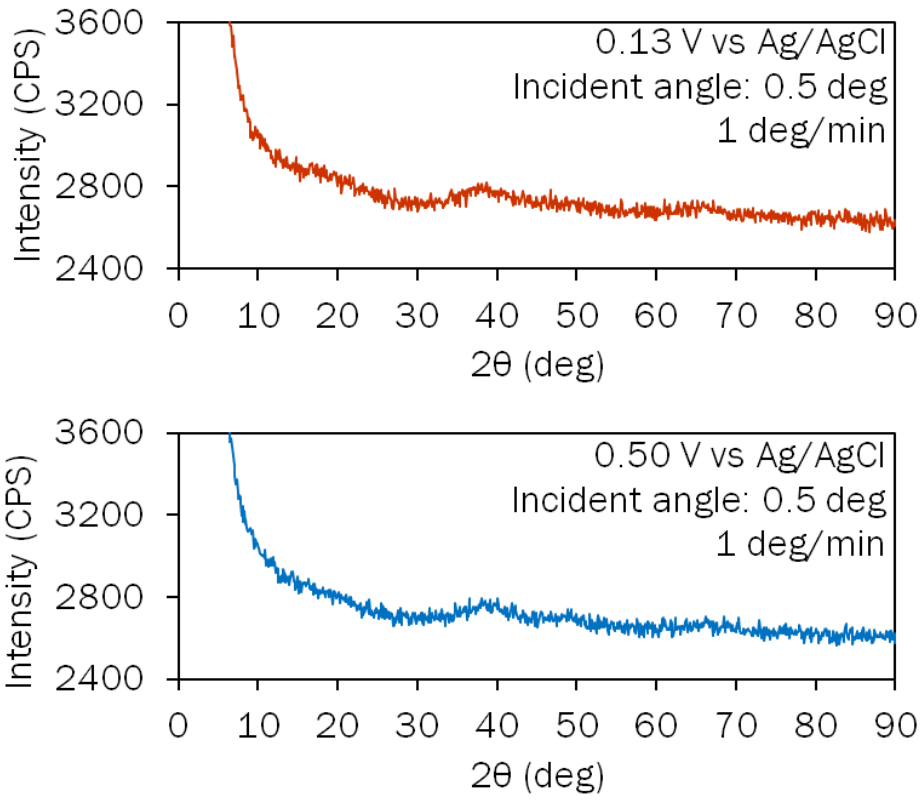

Figure S6. GIXRD on C-O-H oxidized electrochemically under 1 M NaOH by potentials 0.13 and 0.50 V vs Ag/AgCl.

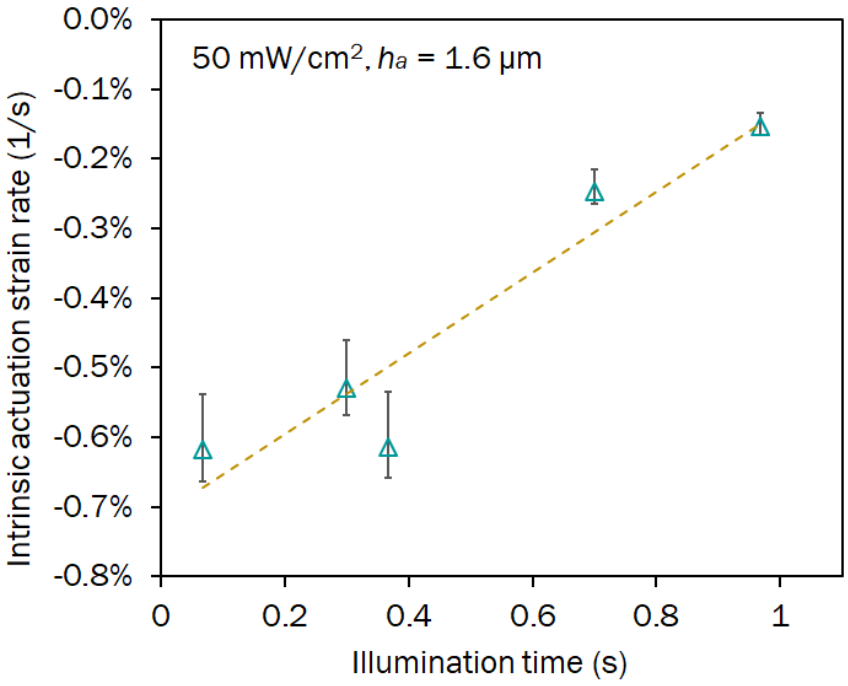

Figure S7. Intrinsic actuation strain rate plotted against illumination time.

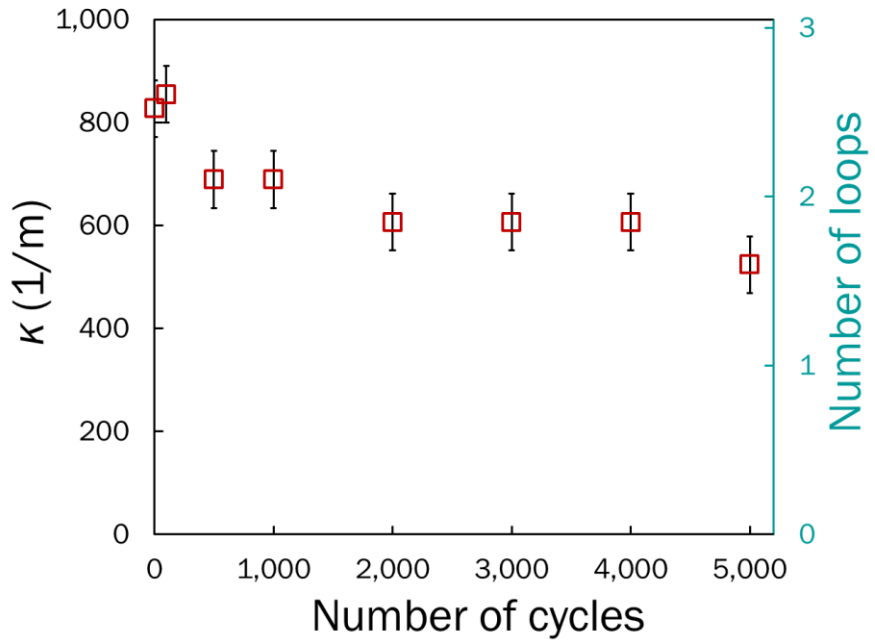

Figure S8. Repeatability cycle test at 20 mW/cm^2 illuminated in 1-s on/4-s off interval for 5000 cycles.

2. Supporting Videos Description

Video S1. Actuation of a C-O-H actuator induced by Vis-light at various intensities

Video S2. Repeatability cycle test

Video S3. Actuation of C-O-H actuators with various h_a

Video S4. Actuation at various relative humidity

Video S5. Heating-induced actuation and actuation induced by illuminating Ni substrate

Video S6. An example Video Showing fast and slow actuation response

Video S7. Weightlifting of C-O-H actuating hinge

Video S8. Weightlifting of an assembly of 3 C-O-H actuators with actuating hinges

Video S9. U-shape hinge for Joule heating-induced actuation

3. Elasticity Model of Light-induced Actuation of C-O-H Bilayer Film Actuator

3a. The whole C-O-H layer is actuated

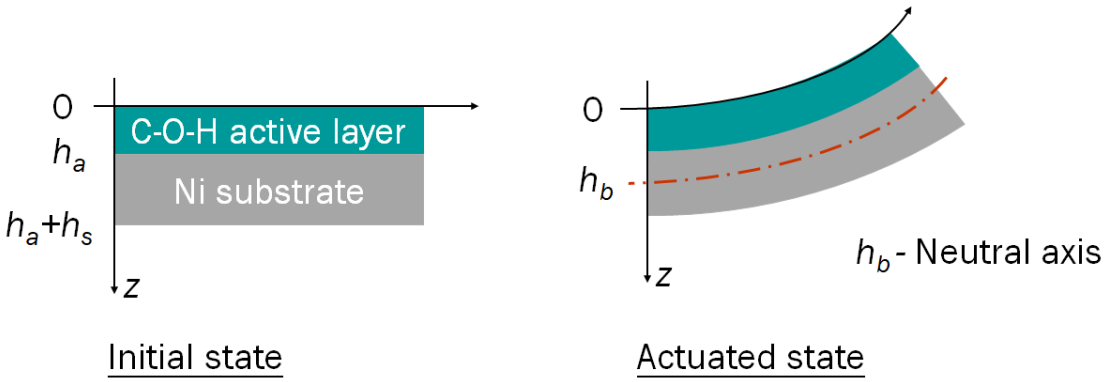

Figure S9. Schematic diagram of the C-O-H bilayer film actuator at initial and actuated state.

The intrinsic actuation performance of C-O-H bilayer film actuator is derived based on Timoshenko's model on bimetal thermostat[6]. In his model, the curvature of thermally induced bending is proportional to the mismatch strain resulted from a different thermal expansion between the two metals. Similarly, the curvature of a C-O-H actuator is caused by the mismatch strain between the active layer C-O-H and the passive Ni substrate.

Under illumination, C-O-H contracts and the film actuator bends as shown in Figure S9. The bent actuator is assumed to have the shape of a circular arc with constant curvature (equal to the reciprocal of the arc radius). The radius is large (>1 mm) compared with the thickness of the actuator cross-section (<10 μm). The thickness of the C-O-H layer is h_a and that of the substrate is h_s. A neutral axis at h_b, defined as the line in the section where the strain is zero, is drawn. The strain, by simple beam bending theory, is given by:

$$\varepsilon = (z - h_b)\kappa, \qquad \text{for } 0 \le z \le h_a + h_s \tag{S1}$$

Equation S1 ensures that each flat plane perpendicular to the beam running across both the active and substrate layers remains flat and perpendicular to the beam after actuation.

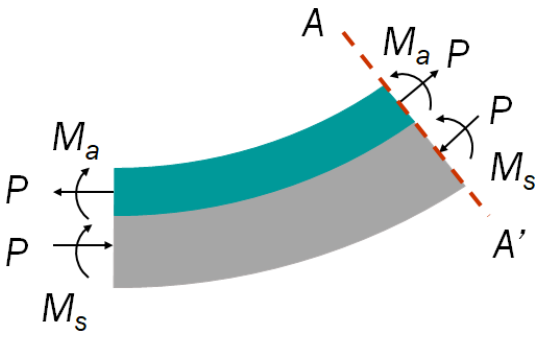

Figure S10. Schematic diagram of force and moment equilibrium at the actuated state

Consider a general cross-section *A-A'* of the composite beam. The active layer produces an actuation force *P* on the substrate. The force couple *P* in section *A-A'* produces a moment $P(h_a + h_s)/2$, which must be equal to the sum of bending moments M_a and M_s (see Figure S10):

$$\frac{P(h_a + h_s)}{2} = M_a + M_s \tag{S2}$$

Note that individually, $Ph_a/2 \neq M_a$ and $Ph_s/2 \neq M_s$. For C-O-H actuator, as the Ni substrate is purely elastic, it can be analysed by standard beam bending theory of combined compression and bending. Shifting the origin of the z coordinate to the mid-plane of the substrate: $z \rightarrow z' = z - (h_a + h_s/2)$, the strain in Equation S1 expressed in z' is: $\varepsilon_s = (z' - h_a - h_s/2 - h_b)\kappa$. Bending moment about the mid-plane of substrate is given by:

$$M_s = E_s \int_{-\frac{h_s}{2}}^{\frac{h_s}{2}} \varepsilon_s z' \, dz' = \frac{E_s h_s^3}{12} \kappa \tag{S3}$$

The active C-O-H layer contracts under stimuli in the actuation, therefore the layer is not purely elastic but "chemo-elastic". The "chemo" actuation strain ε_a^{chem} is a self-inflicted plastic strain. The total average strain of the active layer is given by:

$$\bar{\varepsilon}_a = \varepsilon_a^{chem} + \bar{\varepsilon}_a^{el} = \varepsilon_a^{chem} + \frac{\bar{\sigma}_a}{E_a} \tag{S4}$$

where σ_a is the average actuation stress, and $\bar{\varepsilon}_a$ can also be obtained directly from Equation S1:

$$\bar{\varepsilon}_a = \frac{1}{h_a}\int_0^{h_a}(z-h_b)\kappa dz = \left(\frac{h_a}{2}-h_b\right)\kappa \tag{S5}$$

and hence the strain profile in the actuating layer from Equation S1 is:

$$\varepsilon_a = \bar{\varepsilon}_a + z''\kappa \tag{S6}$$

$$= \varepsilon_a^{chem} + \frac{\bar{\sigma}_a}{E_a} + z''\kappa, \qquad \text{by (S4)}$$

$$= \varepsilon_a^{chem} + \varepsilon_a^{el}, \qquad \text{for } -\frac{h_a}{2} \le z'' \le \frac{h_a}{2}$$

where $z'' = z - h_a/2$ is the coordinate measured from the mid-plane of the active layer, and $\varepsilon_a^{el} = \bar{\sigma}_a/E_a + z''\kappa$ is the elastic component of the strain. In ε_a^{el}, $\bar{\sigma}_a/E_a$ represents the uniform part and $z''\kappa$ the bending part of the elastic strain. Bending moment about the mid-plane of the active layer is:

$$M_a = E_a\int_{-\frac{h_a}{2}}^{\frac{h_a}{2}} \varepsilon_a^{el}\, z''\, dz'' = \frac{E_a h_a^3}{12}\kappa \tag{S7}$$

Hence, from Equation S2, S3 and S7,

$$\frac{P(h_a+h_s)}{2} = \frac{E_a h_a^3 + E_s h_s^3}{12}\kappa \tag{S8}$$

Average actuation stress in active layer is:

$$\bar{\sigma}_a = \frac{P}{h_a} = \frac{E_a h_a^3 + E_s h_s^3}{6h_a(h_a+h_s)}\kappa \tag{S9}$$

Rearranging gives $\kappa = \bar{\sigma}_a[6h_a(h_a+h_s)/(E_a h_a^3 + E_s h_s^3)]$, which reduces to the Stoney Equation[7] as $h_a/h_s \to 0$.

To solve the last unknown h_b, force balance for the substrate is considered:

$$-P = E_s\int_{h_a}^{h_a+h_s}\varepsilon_s\, dz = E_s h_s\left(h_a + \frac{h_s}{2} - h_b\right)\kappa \tag{S10}$$

Therefore,

$$\bar{\sigma}_a = \frac{P}{h_a} = -\frac{h_s E_s}{h_a}\left(\frac{h_s}{2} + h_a - h_b\right)\kappa \tag{S11}$$

Putting Equation S9 into S11:

$$h_b = \frac{E_a h_a^3 + E_s h_s^3}{6E_s h_s (h_a + h_s)} + h_a + \frac{h_s}{2} \tag{S12}$$

which tends to $h_a + 2h_s/3$ as $h_a/h_s \to 0$. Note that force balance for the active layer leads to nothing new:

$$P = E_a \int_{-\frac{h_a}{2}}^{\frac{h_a}{2}} \varepsilon_a^{elastic}\, dz'' = \bar{\sigma}_a h_a \tag{S13}$$

Equating Equation S4 and S5, and substituting in κ and h_b from Equation S9 and S12, we find:

$$\varepsilon_a^{chem} = -\bar{C}_a \bar{\sigma}_a = -K_a \kappa \tag{S14}$$

where

$$\bar{C}_a = \frac{1}{E_a} + \frac{h_a}{E_s h_s} + \frac{3h_a(h_a + h_s)^2}{E_a h_a^3 + E_s h_s^3} \tag{S15}$$

$$K_a = \frac{h_a + h_s}{2} + \frac{E_a h_a^3 + E_s h_s^3}{6(h_a + h_s)} \left(\frac{1}{E_a h_a} + \frac{1}{E_s h_s} \right)$$

Equation S14 gives the chemo-strain ε_a^{chem} needed to produce a given $\bar{\sigma}_a$or κ. Note that ε_a^{chem} needs to be compressive in order to generate a tensile $\bar{\sigma}_a$ or positive κ in the sense defined, which should indeed be the case. The coefficient K_a has the same format as given by Timoshenko[6], where $-\varepsilon_a^{chem}$ plays the role of a "mismatch strain". The actuating work density is given as:

$$W_a = -\int \bar{\sigma}_a d\varepsilon_a^{chem} = \bar{C}_a \int \bar{\sigma}_a d\bar{\sigma}_a = \frac{\bar{C}_a\, \bar{\sigma}_a^2}{2} \tag{S16}$$

Figure S11 is a theoretical plot of K_a against h_a, using the current values of h_s = 1.2 μm, E_a = 17.0 GPa, and E_s = 220 GPa (E_a/E_s = 0.077). It shows that at a given intrinsic strain ε_a^{chem}, Equation S14 predicts that κ will first increase (the bilayer will become curlier) with h_a to a peak and then decrease, due to the change of bending-dominated to stretching-dominated deformation of the bilayer. If C-O-H is much thicker than the substrate ($h_a \gg h_s$), the bilayer essentially becomes a bulk C-O-H and therefore linear deformation is resulted.

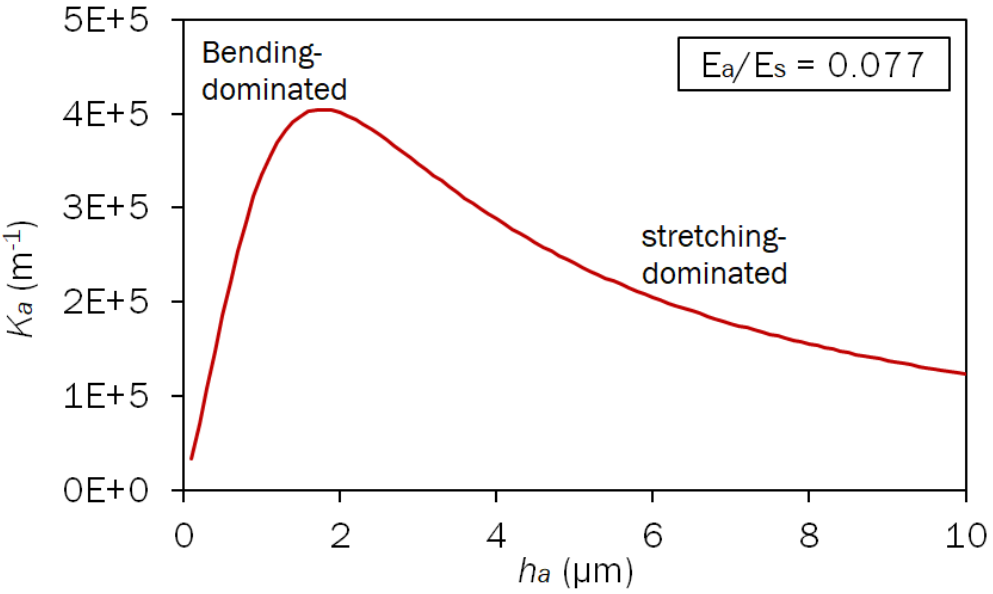

Figure S11. Theoretical curve of $K_a = -\kappa/\varepsilon_a^{chem}$ against h_a with E_a/E_s = 0.077.

To see the actuation performance of our C-O-H actuator, κ, ε_a^{chem} and $\bar{\sigma}_a$, are plotted against h_a in Figure S12. The major observations are as follows:

(1) For κ, the value first increases with h_a in the small-h_a regime and then decreases to a constant value (Figure S12a). Defining the effectiveness of actuation to be κ/h_a, the curve in Figure S12b monotonically decreases with h_a. This means that the increase in h_a will not increase κ proportionately in the small-h_a regime. The highest effectiveness is achieved at the lowest h_a.

(2) For ε_a^{chem} (Figure S12c), at 10 and 20 mW/cm^2, the value is fairly constant at small to medium h_a and increases slightly at the two largest h_a values; however, at 50 mW/cm^2, a significant increase in ε_a^{chem} with h_a is found, from -0.54% to -1.29%. This might be caused by the more complete actuation induced at the high light intensity. Comparing with Figure S12a, the difference in the trends of ε_a^{chem} and κ is due to the change of bending-dominated to stretching-dominated deformation described above. The ratio of $\bar{\sigma}_a/\varepsilon_a^{chem} = -1/\bar{C}_a$ is plotted in Figure 12d, with two exceptionally large hypothetical

h_a plotted. This shows that at large h_a (from 4.2 – 9.4 μm), $\bar{\sigma}_a/\varepsilon_a^{chem}$ is approximately constant (independent of h_a or κ), because the deformation is stretching-dominated. Hence, the curves in Figure 1h lie on a straight line with a slope of about -3000 MPa. At low h_a, $-1/\bar{C}_a$ increases linearly, meaning that for a constant or slightly increasing intrinsic actuation strain ε_a^{chem}, the average stress $\bar{\sigma}_a$ will decrease due to the averaging effect of tensile and compressive stress as discussed below.

(3) For $\bar{\sigma}_a$ (Figure S12e), the value is the highest at the smallest h_a, which decreases rapidly in the small h_a regime to a constant value in the medium h_a regime. This is because $\bar{\sigma}_a$ is an average value of the stress state along the thickness direction (z) of C-O-H. The stress of C-O-H (σ) at any z is given by

$$\sigma = E_a(\varepsilon - \varepsilon_a^{chem}) \tag{S17}$$

$$= E_a[(z - h_b)\kappa - \varepsilon_a^{chem}], \qquad \text{by Equation S1}$$

Note that

$$\bar{\sigma}_a = \frac{1}{h_a}\int_0^{h_a} \sigma dz = E_a\left[\left(\frac{h_a}{2} - h_b\right)\kappa - \varepsilon_a^{chem}\right] \tag{S18}$$

$$= \frac{E_a h_a^3 + E_s h_s^3}{6h_a(h_a + h_s)}\kappa, \qquad \text{which is Equation S9}$$

As shown in Figure S12f, σ at surface (z=0) experiences a change from tensile to compressive and that at the interface ($z = h_a$) and the average stress $\bar{\sigma}_a$ are always tensile at 50 mW/cm^2. As is more clearly shown in Figure S13, at small h_a (<1.6 μm), only tensile stress is found along z (represented by fraction of C-O-H thickness), with the magnitude decreasing from the interface $z = h_a$ (thickness fraction = 0) to surface z = 0 (thickness fraction = 1). At larger h_a (≥2 μm), compressive stress appears on the C-O-H surface. Therefore, at small to medium h_a where ε_a^{chem} is fairly constant, the average actuating stress $\bar{\sigma}_a$ drops significantly as shown in Figure S12f. However, as ε_a^{chem} increases significantly at large h_a, it wins over the averaging effect and causes

$\bar{\sigma}_a$ to increase. (σ at $z = 0$ is proportional to ε_a^{chem}). Therefore, at the largest two h_a tested, $\bar{\sigma}_a$ increases slightly and matches the trend of ε_a^{chem}. This explains the difference in trend between $\bar{\sigma}_a$ and the self-inflicted actuation strain ε_a^{chem}.

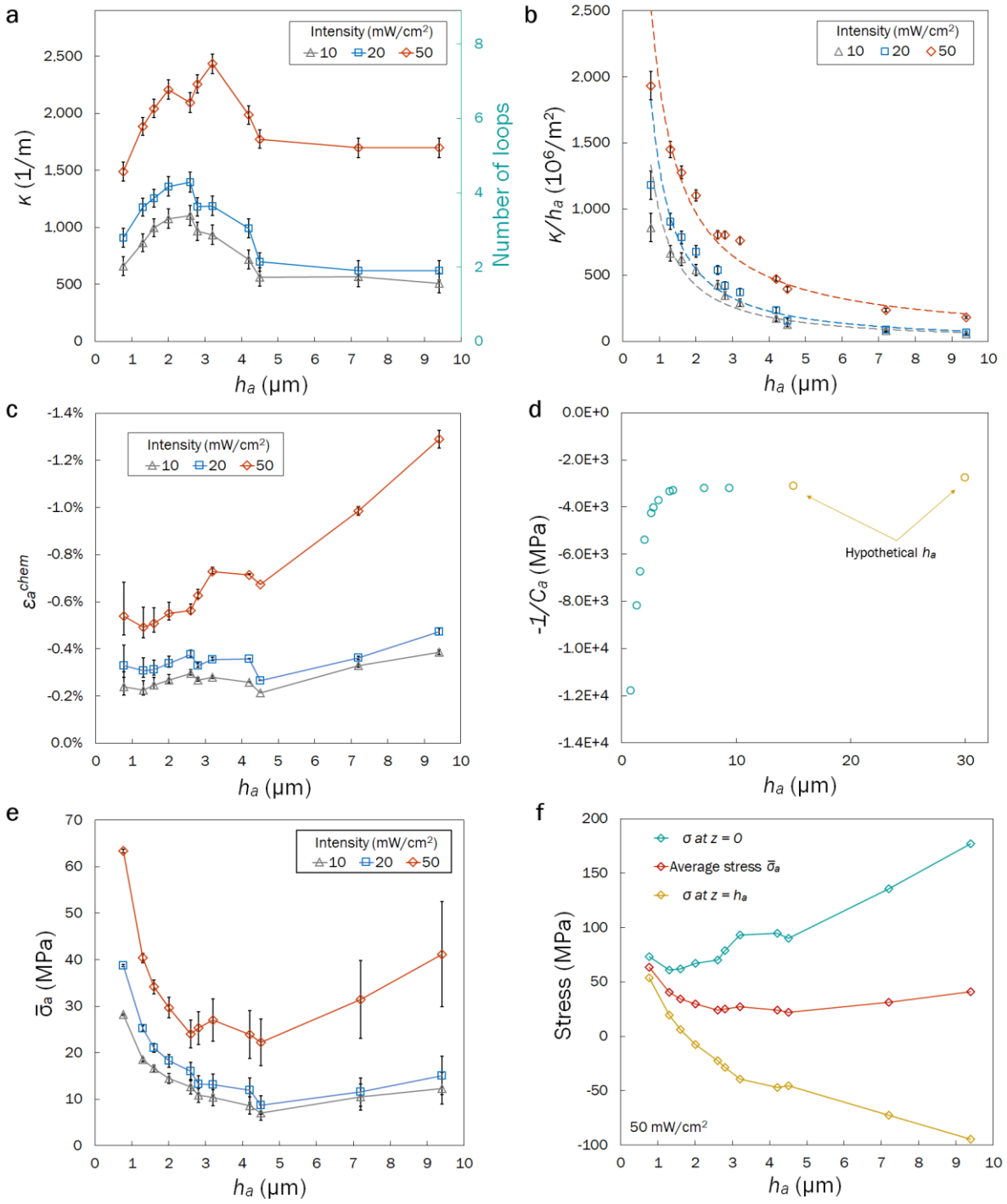

Figure S12. Various plots against h_a: a) curvature κ, b) actuation effectiveness κ/h_a, c) intrinsic actuation strain ε_a^{chem}, d) $\bar{\sigma}_a/\varepsilon_a^{chem} = -1/\bar{C}_a$, e) average actuation stress $\bar{\sigma}_a$, and f) stress σ at interface ($z = h_a$), surface ($z = 0$) and average stress $\bar{\sigma}_a$.

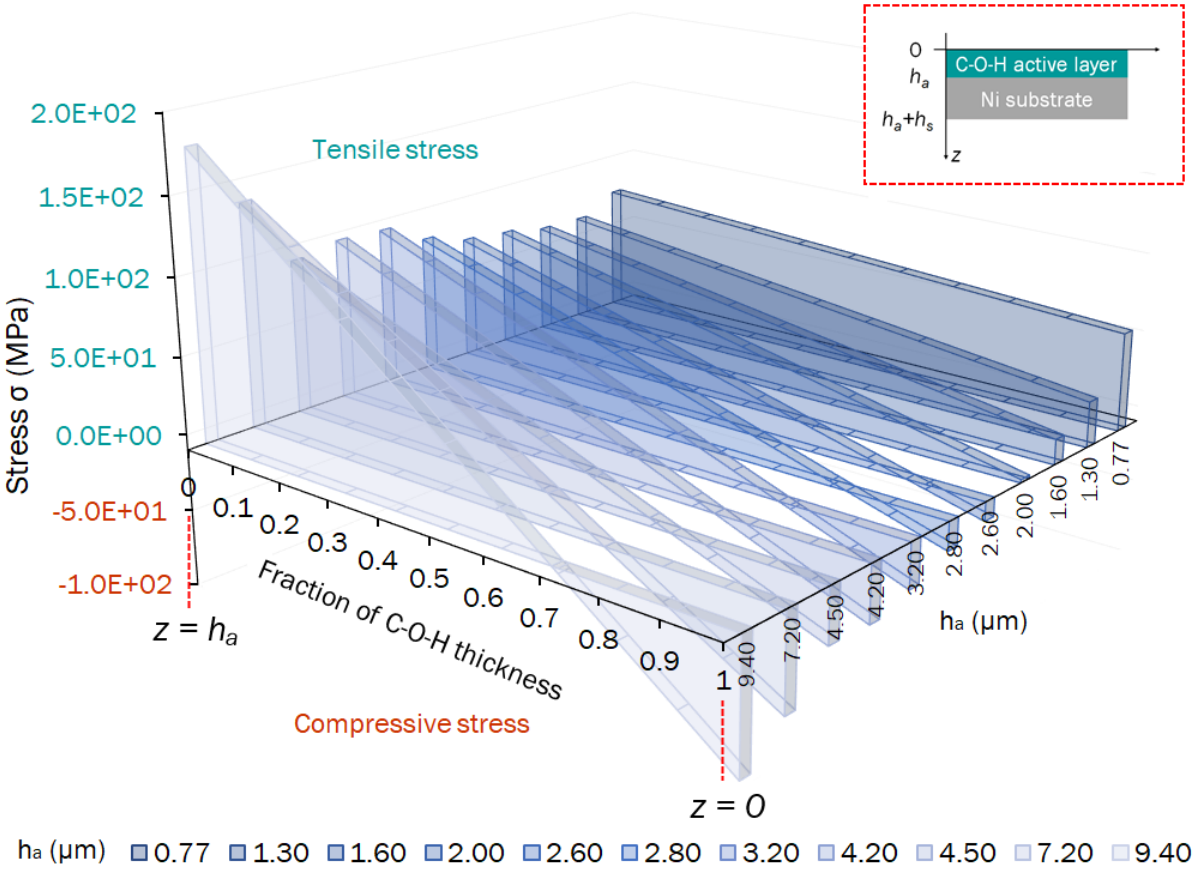

Figure S13. Stress state of C-O-H along its thickness at various h_a.

3b. Only a small depth of C-O-H layer is immediately triggered by Vis-light

As shown in Figure S14, actuation can be induced by lowering the relative humidity.

With the test results in Figure 2, the actuation mechanism is deduced to be water desorption from C-O-H. Observed from experiments, the actuation of C-O-H actuator exhibits an initial fast response followed by a slow response (inset in Figure 2e). While the fast actuation part is almost immediately triggered, the slow part should be diffusion-controlled, as confirmed in Figure 2e where the square root of total actuation time is proportional to h_a, obeying a characteristic of diffusion. Therefore, the actuated state in Figure S10 can be redrawn as Figure S15, in which an immediately triggered layer (orange) with thickness h_t quickly responds (by water desorption and volume shrinkage) at the moment of illumination. The water concentration is quickly set to a value c_s, driving the diffusion in the remaining blue layer which has an initial water concentration c_0 ($> c_s$).

Figure S14. The shape of the actuator at different relative humidity (scale bar: 10 mm).

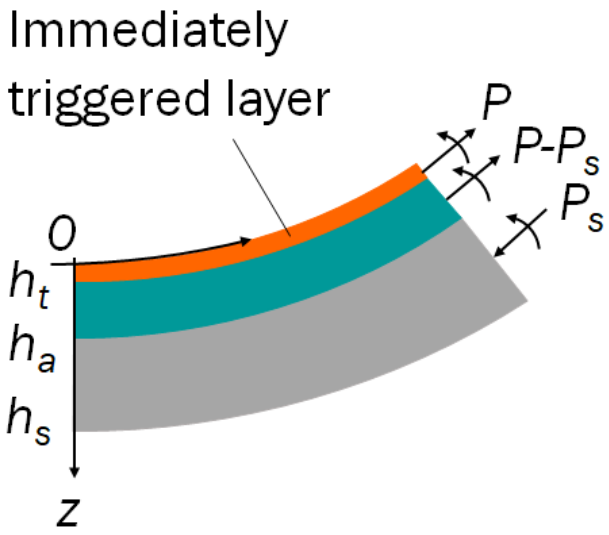

Figure S15. Schematic of the actuated state with a spontaneous triggered layer and a diffusion-controlled layer.

At any time t after diffusion has started in the active layer, the profile of the water concentration c is given by the solution to Fick's second law:

$$c(z',t) = (c_0 - c_s)\,\mathrm{erf}\left(\frac{z'}{2\sqrt{Dt}}\right) + c_s \tag{S19}$$

where z' is the coordinate measured from the interface between the orange and blue layers, and D is the diffusion coefficient of water in C-O-H. As t increases, the $c(z',t)$ profile changes and eventually, the water concentration in the blue layer will drop to close to c_s, and then the actuation will stop. This "eventual actuation time" t_a can be taken to be the time for the concentration at $z' = h_a - h_t$ to reach, say, $1.1c_s$, so, from Equation S19, t_a is given by:

$$t_a = \frac{(h_a - h_t)^2}{D}\frac{1}{\left[\mathrm{erf}^{-1}\left(\frac{0.1c_s}{c_0 - c_s}\right)\right]^2} \approx \frac{(h_a - h_t)^2}{4D}\left(\frac{c_0 - c_s}{0.1c_s}\right)^2 \propto \frac{(h_a - h_t)^2}{4D} \tag{S20}$$

The straight-line trend in Figure 2e does not pass through the origin, indicating a value of h_t on the order of one micron.

The non-triggered C-O-H layer is under a force of $P - P_s$ in this state. The remaining active layer (green, with thickness $h_a - h_t$) becomes the diffusion layer, where diffusion will start when the spontaneous triggered layer (orange) has its water concentration reduced due to the light illumination, resulting a concentration difference between the two layers.

Similar to Equation S2, the moment over a cross section must be balanced. Taking moment about the mid-plane of the green layer gives:

$$\frac{Ph_a}{2} + \frac{P_s(h_a + h_s - h_t)}{2} = \frac{\kappa}{12}[E_a h_t^3 + E_a(h_a - h_t)^3 + E_s h_s^3] \tag{S21}$$

Strain is still that in Equation S1. Force balance of the substrate layer gives:

$$-P_s = E_s \int_{h_a}^{h_a+h_s} (z - h_b)\kappa \, dz' = E_s h_s \left(h_a + \frac{h_s}{2} - h_b\right)\kappa \tag{S22}$$

Substituting Equation S22 into S21, and writing actuating stress as $\bar{\sigma}_a = P/h_t$:

$$\bar{\sigma}_a = \frac{\kappa}{6h_a h_t}\{E_a[h_t^3 + (h_a - h_t)^3] + E_s h_s^3\} + \frac{E_s h_s \kappa}{h_a h_t}\left(h_a + \frac{h_s}{2} - h_b\right)(h_a + h_s - h_t) \tag{S23}$$

As shown in Figure S16, force balance of the green layer (non-triggered C-O-H) gives:

$$-(P - P_s) = E_a \int_{h_t}^{h_a} (z - h_b)\kappa \, dz = \kappa E_a (h_a - h_t)\left(\frac{h_a + h_t}{2} - h_b\right) \tag{S24}$$

Substituting Equation S22 into S24:

$$\bar{\sigma}_a = \kappa E_s \frac{h_s}{h_t}\left(h_b - h_a - \frac{h_s}{2}\right) + \kappa E_a \left(\frac{h_a}{h_t} - 1\right)\left(h_b - \frac{h_a + h_t}{2}\right) \tag{S25}$$

Eliminating h_b between Equation S23 and S25, and simplifying, give:

$$\bar{\sigma}_a = \kappa \frac{\Delta E(E_a h_a^4 - E_s h_s^4) + E_a E_s h^4 + h_t E_a(-4Y_3 + 6h_t Y_2 - 3h_t^2 Y_1)}{6h_t(Y_2 - h_t Y_1)} \tag{S26}$$

where $\Delta E = E_a - E_s$; $h = h_a + h_s$; $Y_n = \Delta E \, h_a^n + E_s \, h^n$. If $h_t = h_a$, then Equation S26 reduces to Equation S9. Equation S26 is only applicable before diffusion is significant, and the curvature would be measured by only considering the fast actuation (κ_{fast}). In the example in Figure S15, κ_{fast} is taken as 644 m^{-1} at illumination time of 1 s, beyond which the actuation

slows down significantly. To estimate the actuation stress due to the immediately triggered actuation ($\bar{\sigma}_{a_{fast}}$), the triggered layer thickness h_t has to be determined. Rewriting Equation S26 as:

$$\frac{\kappa_{fast}}{\bar{\sigma}_{a_{fast}}} = \frac{6h_t(Y_2 - h_t Y_1)}{X + h_t E_a(-4Y_3 + 6h_t Y_2 - 3h_t^2 Y_1)} \quad \text{(S27)}$$

where $X = \Delta E(E_a h_a^4 - E_s h_s^4) + E_a E_s h^4$, $h = h_a + h_s$, and plotting κ_{fast} at 50 mW/cm^2 against $\frac{6h_t(Y_2 - h_t Y_1)}{X + h_t E_a(-4Y_3 + 6h_t Y_2 - 3h_t^2 Y_1)}$ (Figure 2f), h_t can be determined as the value that gives the plot the best linearity. The coefficient of correlation R^2 of the proportional fit is maximized with respect to h_t, giving h_t = 1.36 μm and the corresponding slope of the fitting line $\bar{\sigma}_{a_{fast}}$ = 33.2 MPa, which agrees in magnitude with $\bar{\sigma}_a$ in Figure 1h.

4. Chemo-mechanics Model

4a. Chemo-driven actuation stress-strain characteristics

The actuation of C-O-H can be described by the reaction:

$$\text{C-O-H (water desorbed)} \rightleftharpoons \text{C-O-H (water adsorbed)} \tag{S28}$$

where the LHS has a smaller volume than the RHS. The forward and backward reaction rate are given by:

$$\overrightarrow{\text{rate}} = [C_s]\exp\left(-\frac{E_f}{kT}\right), \overleftarrow{\text{rate}} = [C_l]\exp\left(-\frac{E_b}{kT}\right) \tag{S29}$$

where $[C_s]$ and $[C_l]$ are the concentration of C-O-H (water desorbed) and C-O-H (water adsorbed), and E_f and E_b the activation energy of forward and backward reaction. The activation energies are shown in Figure 4a, and $E_f - E_b = -(\Delta E_{chem} - \sigma_a \Omega)$ where ΔE_{chem} is the chemical driving force for the reaction towards C-O-H (water desorbed), and σ_a is the stress in C-O-H.

At equilibrium, the two rates in Equation S29 are equal, so that

$$(1 + 3\varepsilon_a^{chem}) = K_{eq} = \frac{[C_l]}{[C_s]} = \exp\left(-\frac{\Delta E_{chem} - \sigma_a \Omega}{kT}\right) \tag{S30}$$

The concentration ratio $[C_l]/[C_s]$ determines the volume and may be written as $(1 + 3\varepsilon_a^{chem})$ where the state $[C_l] = [C_s]$ (i.e. the mid-point of reaction in Equation S28) is taken as the reference state and $\varepsilon_a^{chem} (\ll 1)$ is the actuation strain from such a state. Therefore, Equation S30 can be rewritten as

$$\sigma_a \Omega \approx \Delta E_{chem} + kT \ln(1 + 3\varepsilon_a^{chem}) \approx \Delta E_{chem} + 3kT\varepsilon_a^{chem} \tag{S31}$$

which represents the actuation stress-strain characteristics of C-O-H.

4b. Chemo-diffusion equilibrium

For $h_a \gg h_t$, the rate of the actuator response is mainly controlled by diffusion in the green layer in Figure S15. However, equilibrium is established when the chemical potential of water molecules in the green (diffusion) layer balances that in the orange (triggered) layer. Chemical potential for diffusion is in general given as: $\mu = \mu_0 - \sigma\Omega + kT \ln c$, where μ_0 is a reference potential, c is concentration of the diffusing species, σ is tensile stress and Ω is an activation volume. For the present problem, let c_t, c_d be the concentration of water in the triggered (orange) and diffusive (green) layer, σ_t, σ_d be the tensile stress in the triggered (orange) and diffusive (green) layer, and Ω_t, Ω_d be the activation volume in the triggered (orange) and diffusive (green) layer. The chemical potential of water in the triggered layer relative to the environment outside is:

$$\mu_t = \Delta E_{chem} + \mu_0 - \sigma_t \Omega_t + kT \ln c_t \tag{S32}$$

At equilibrium with the environment, $\mu_t = 0$, and so:

$$\ln c_t = -(\Delta E_{chem} + \mu_0 - \sigma_t \Omega_t)/kT \tag{S33}$$

Defining $c_0 = \exp(-\mu_0/kT)$ as the equilibrium water concentration in the stress-free ($\sigma_t = 0$), unstimulated ($\Delta E_{chem} = 0$) state of the active material, then

$$\ln(c_t/c_0) = -(\Delta E_{chem} - \sigma_t \Omega_t)/kT \tag{S34}$$

As the triggered layer and the diffusion layer are of the same material, their reference potential must be the same, and so at equilibrium, equalization of their potentials leads to:

$$kT \ln c_t - \sigma_t \Omega_t = kT \ln c_d - \sigma_d \Omega_d \tag{S35}$$

From Equation S34,

$$\ln(c_d/c_0) = -(\Delta E_{chem} - \sigma_d \Omega_d)/kT \quad \text{(S36)}$$

Equation S36 appears the same as Equation S34, and both equations say that in either layers, the concentration of water is determined by the same overall driving force ΔE_{chem} due to the stimulus on the triggered layer, and the local stress potential $\sigma_t \Omega_t$ or $\sigma_d \Omega_d$ in the layer. Equation S34 and S36 are really S30 or S31 in which c_t/c_0 or c_d/c_0 plays the role of $(1 + 3\varepsilon_a^{chem})$, i.e. Equation S31 is also applicable to the diffusive layer at equilibrium, as it is applicable to the triggered layer. Therefore, even though the rate of the actuation response is controlled by the diffusion kinetics in the non-triggered part of the active material layer, at eventual equilibrium when diffusion has stopped, the stress-strain relation is still governed by Equation S31, with the same driving force ΔE_{chem} as for the triggered layer. This is not surprising, since diffusion is only the kinetic process of water transport from the green layer to the orange layer when there is a concentration difference between the two, and then from the orange layer to the environment outside, the water is by the stimulus under driving force ΔE_{chem}. As mentioned above, the green and orange layers are of the same material and so the diffusion between them is associated with no intrinsic driving force other than a difference in the extrinsic potential ($kT \ln c - \sigma\Omega$). ΔE_{chem} is the one and only one driving force in the whole system, and this is why Equation S31 with one ΔE_{chem} is applicable to both the triggered and diffusion layers.

4c. Chemo-mechanics equilibrium

At chemo-mechanics equilibrium, the chemical actuation stress-strain characteristics in Equation S31 should balance the mechanical characteristics arising from the rigidity response of the active and substrate layers. Equation S14 gives the relation between ε_a^{chem} and the average actuating stress $\bar{\sigma}_a$ in the active layer; however, the chemo-relation in Equation S31 should apply to the top-surface layer of the active material at which the stress is $\sigma_a = \sigma(z = 0)$ used. From Equation S17,

$$\sigma_a \coloneqq \sigma(z=0) = E_a\left(-h_b\kappa - \varepsilon_a^{chem}\right) = \left[\frac{E_a h_a^3 + E_s h_s^3}{6h_a(h_a+h_s)} - \frac{E_a\, h_a}{2}\right]\kappa \tag{S37}$$

so that

$$\sigma_a = -\varepsilon_a^{chem}/C_a \tag{S38}$$

where

$$C_a = \frac{K_a}{\left[\frac{E_a h_a^3 + E_s h_s^3}{6h_a(h_a+h_s)} - \frac{E_a\, h_a}{2}\right]} = \frac{\frac{(h_a+h_s)}{2} + \frac{E_a h_a^3 + E_s h_s^3}{6(h_a+h_s)}\left(\frac{1}{E_a h_a} + \frac{1}{E_s h_s}\right)}{\frac{E_a h_a^3 + E_s h_s^3}{6h_a(h_a+h_s)} - \frac{E_a\, h_a}{2}} \tag{S39}$$

When the top surface is at chemo-mechanical equilibrium, Equation S31) and S38 must be satisfied together as shown in Figure S16.

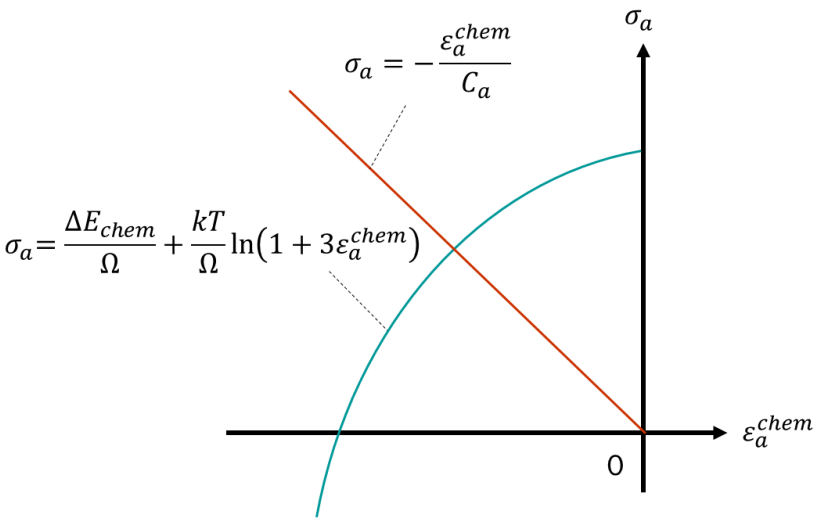

Figure S16. Sketch on the Equation S31 and S38 showing the chemo-mechanical equilibrium.

Therefore,

$$\sigma_a = \frac{\Delta E_{chem}}{\Omega + 3kTC_a} \tag{S40}$$

From Equation S14, S38 and S40, we can define a normalized curvature as:

$$K = \frac{\kappa(E_s h_s^3)^{1/3}}{\phi E_a^{1/3}} = \frac{\kappa h_s}{\phi \beta^{1/3}} \tag{S41}$$

$$= \frac{6\alpha\beta^{2/3}(1+\alpha)}{(1+\alpha\beta)(1+\alpha^3\beta)+\omega[1-\alpha^2\beta(3+2\alpha)]+3\alpha\beta(1+\alpha)^2}$$

where $\alpha = h_a/h_s$, $\beta = E_a/E_s$, $\phi = \Delta E_{chem}/(3kT)$, and $\omega = E_a\Omega/(3kT)$. K here is a normalized measure for curvature performance because a higher K means (i) higher substrate bending stiffness $E_s h_s^3$ for the same curvature κ, (ii) higher curvature κ for the same substrate bending stiffness $E_s h_s^3$, (iii) lower driving force ϕ needed for the same curvature and substrate bending stiffness. The parameters ϕ and ω are normalized measures for the thermodynamic driving force ΔE_{chem}, and the activation volume Ω, respectively, and hence they are figures of merit of the activation material. In particular, ϕ directly indicates the magnitude of the thermodynamic driving force for the actuation provided by the stimulation, and hence it is a

more important figure of merit. The chemo characteristics of the actuation in Equation S31 can also be recast in these two parameters as:

$$\varepsilon_a^{chem} = \left(\frac{\sigma_a}{E_a}\right)\omega - \phi \tag{S42}$$

From Equation S42, it can be seen that the normalized driving ϕ is also the stress-free actuation strain, i.e. $\phi = -\varepsilon_a^{chem}(\sigma_a = 0)$. Plotting ε_a^{chem} against σ_a/E_a would yield ω as the slope and ϕ as the minus of the *y*-intercept.

The data points of ε_a^{chem} and $\bar{\sigma}_a$ in Figure 1h are replotted with those measured and calculated from another actuating materials nickel hydroxide-oxyhydroxide (NHO)[8] fabricated for comparison (Figure S17a). It can be seen that C-O-H is a more effective actuating material than NHO, as it produces larger $\bar{\sigma}_a$ over wider ε_a^{chem} at the same light intensity. Figure S17b shows the plots of ε_a^{chem} against σ_a/E_a for comparison with the chemical characteristics in Equation S42; in particular, the *y*-intercept gives the normalized driving force ϕ, and the slope of the plot gives the normalized activation volume ω. For a given light intensity, C-O-H has higher ϕ than NHO.

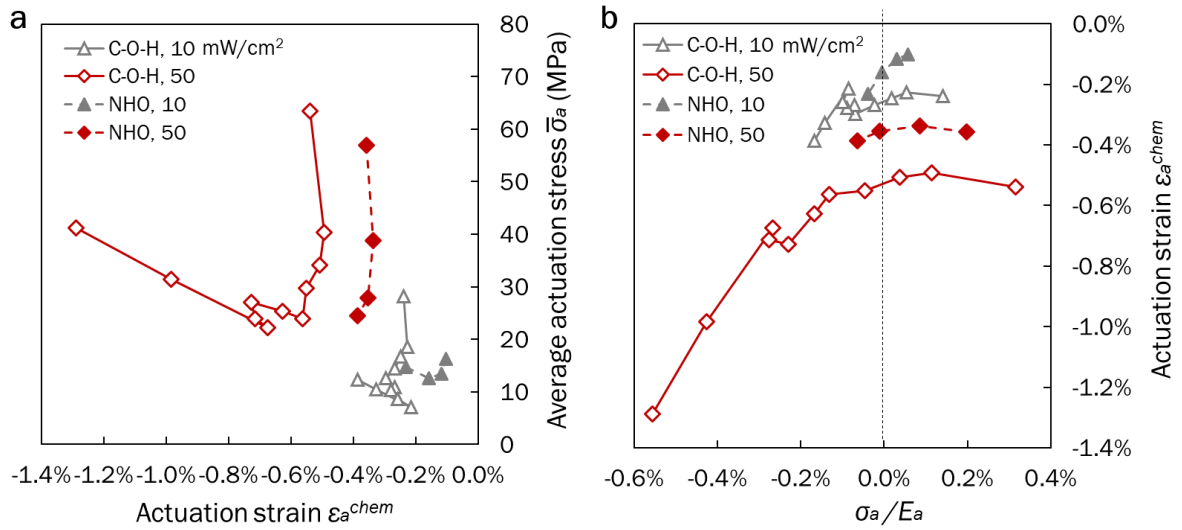

Figure S17. a) $\bar{\sigma}_a$ versus ε_a^{chem}; b) ε_a^{chem} versus σ_a/E_a, showing how ϕ and ω can be determined from the intercept and slope.

As for the normalized activaton volume ω, it can be seen from Figure S17b that the ε_a^{chem} versus σ_a/E_a plots are rather nonlinear, but the range of variation of the slope is not dissimilar between C-O-H and NHO at different intensities. In fact, from the definition $\omega = E_a\Omega/(3kT)$, C-O-H and NHO have rather similar E_a values of 17 GPa and 24 GPa respectively, or β values of 0.077 and 0.11 respectively (E_s for Ni substrate is 220 GPa).Figure 4c shows C-O-H has much higher ϕ than NHO. Therefore, although the two material systems have rather similar $K(\alpha)$ because their β and ω values are similar, the much higher ϕ for C-O-H means that the actuation curvature κ is also much higher for C-O-H at the same thickness ratio and light intensity as K is defined as $\kappa h_s/(\phi\beta^{1/3})$.

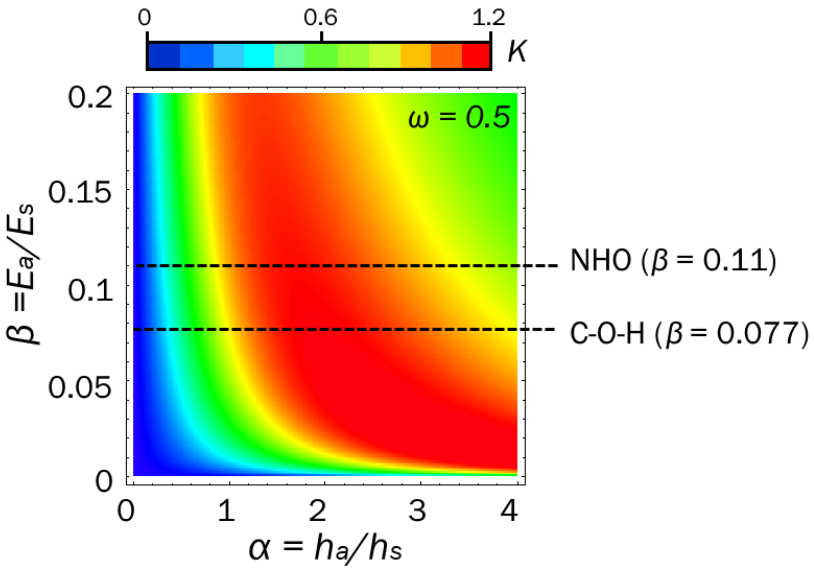

Figure S18. Theoretical plot of $K(\alpha, \beta)$ for ω = 0.5 as per Equation 7, showing the operating conditions for C-O-H and NHO.

5. References

[1] K. Persson, *Materials Data on Co(HO)2 (SG:5) by Materials Project*, https://materialsproject.org/materials/mp-625953/

[2] K. Persson, *Materials Data on CoHO2 (SG:166) by Materials Project*, https://materialsproject.org/materials/mp-31526/

[3] K. Persson, *Materials Data on Co3O4 (SG:227) by Materials Project*, https://materialsproject.org/materials/mp-18748/

[4] A. a. O. Jain, Shyue Ping and Hautier, Geoffroy and Chen, Wei and Richards, William Davidson and Dacek, Stephen and Cholia, Shreyas and Gunter, Dan and Skinner, David and Ceder, Gerbrand and Persson, Kristin a., *APL Mater.* **2013**, *1*, 011002.

[5] H. G. Meier, J. Vilche, A. Arvia, *J. Electroanal. Chem.* **1982**, *138*, 367.

[6] S. Timoshenko, *Josa* **1925**, *11*, 233.

[7] G. G. Stoney, *Proceedings of the Royal Society of London. Series A, Containing Papers of a Mathematical and Physical Character* **1909**, *82*, 172.

[8] K. Kwan, S. Li, N. Hau, W.-D. Li, S. Feng, A. H. Ngan, *Sci. Robot.* **2018**, *3*, eaat4051.